

# Perturbative renormalization group approach to magic-angle twisted bilayer graphene using topological heavy fermion model

Yi Huang,\* Yang-Zhi Chou, and Sankar Das Sarma

Condensed Matter Theory Center and Joint Quantum Institute,

Department of Physics, University of Maryland, College Park, Maryland 20742, USA

We develop a perturbative renormalization group (RG) theory for the topological heavy fermion (THF) model, describing magic-angle twisted bilayer graphene (MATBG) as an emergent Anderson lattice. The realistic parameters place MATBG near an intermediate regime where the Hubbard interaction  $U$  and the hybridization energy  $\gamma$  are comparable, motivating the need for RG analysis. Our approach analytically tracks the flow of single-particle parameters and Coulomb interactions within an energy window below 0.1 eV, providing implications for distinguishing between Kondo-like ( $U \gg \gamma$ ) and projected-limit/Mott-semimetal ( $U \ll \gamma$ ) scenarios at low energies. We show that the RG flows generically lower the ratio  $U/\gamma$  and drive MATBG toward the chiral limit, consistent with the previous numerical study based on the Bistritzer-MacDonald model. The framework presented here also applies to other moiré systems and stoichiometric materials that admit a THF description, including magic-angle twisted trilayer graphene, twisted checkerboard model, and Lieb lattice, among others, providing a foundation for developing low-energy effective theories relevant to a broad class of topological flat-band materials.

## I. INTRODUCTION

Magic-angle twisted bilayer graphene (MATBG) is a prime platform for studying strongly correlated physics in a topologically nontrivial band structure. Its nearly flat moiré bands at the magic angle, where the interlayer tunneling is equal to the moiré momentum displacement multiplied by graphene Dirac velocity, lead to interaction-driven phases including correlated insulators and superconductivity [1–33]. Meanwhile, electronically modeling the flat band in MATBG has faced a fundamental challenge: an isolated flat band in MATBG cannot be described by a tight-binding model due to its topological character and long-range (power-law) Wannier tails. Two notable categories of approaches have been proposed to resolve the Wannier obstruction: earlier methods that include many remote bands, and the recently introduced topological heavy fermion (THF) model [34–36]. The first approach is to combine the flat bands with a few remote bands calculated from Bistritzer-MacDonald (BM) model [37] such that the whole set of bands is topologically trivial [38–41]. The second approach is the THF model [34–36], which maps the low-energy physics onto an Anderson–lattice-like problem [42, 43] of  $f$ -orbitals localized in moiré lattice hybridizing with dispersive  $c$ -electrons, opening the prospect of applying heavy-fermion physics tools to MATBG. The THF model provides a conceptually clear division: the localized  $f$ -fermions (flat-band states with completely quenched kinetic energy, centered on AA sites) carry Hubbard-like Coulomb repulsion, while the itinerant  $c$ -fermions (Dirac-like extended states carrying nontrivial Berry curvature) carry the band topology. The topological flat bands emerge from a band inversion (hybridization) between the  $f$ - and  $c$ -orbitals. Unlike the first approach, which incorporates a few remote bands to resolve the Wannier obstruction, the THF model achieves this by selectively hybridizing only part of the remote-band states near the  $\Gamma$  point with the flat bands.

This yields a minimal, analytically tractable, and physically motivated basis of  $c$ - and  $f$ -fermions, capturing the essential topological and interaction-driven physics without involving the full remote-band manifold [44].

Compared with the numerically intensive BM model, the THF model, parameterized by fitting only a few key quantities—such as the  $c$ -fermion velocity  $v_*$ ,  $cf$ -hybridization strength  $\gamma$ , and flat-band width  $M$ —offers significant analytical advantages for understanding MATBG’s low-energy properties below  $v_*\Lambda_c \simeq 100$  meV. See Fig. 1.  $\Lambda_c$  is the scale set by the first moiré Brillouin zone (mBZ) and  $v_*\Lambda_c$  defines the bandwidth of the  $c$ -fermions. Specifically, the THF model enables analytical derivations of the flat-band wavefunctions and associated Berry curvature [34, 45]. Furthermore, projecting the Coulomb interaction onto the THF single-particle basis naturally disentangles the interactions into clearly defined physical channels. These include Hubbard-like onsite repulsion ( $U$ ) among  $f$ -fermions, density-density interactions within itinerant  $c$ -fermions ( $V$ ), density-density interactions between localized and itinerant fermions ( $W$ ), exchange coupling ( $J$ ), and double-hybridization processes ( $J_+$ ) [34]. This decomposition facilitates a transparent interpretation and systematic exploration of correlation effects in MATBG.

An essential question in interacting MATBG is the relative energy scale hierarchy between  $U$ ,  $\gamma$ , and  $M$ . Given that  $\gamma$  characterizes the gap between flat and remote bands in the THF model, the existence of flat bands naturally implies  $\gamma \gg M$ . See Fig. 2 (a). We focus on the strongly correlated regime of the flat band, while the dispersive bands remain in the perturbative regime, characterized by the hierarchy  $v_*\Lambda_c \gg U \gg M$ . Within this regime, two distinct scenarios emerge depending on the relative strength of  $U$  and  $\gamma$ : either  $U \gg \gamma$  or  $U \ll \gamma$ . See Fig. 2 (b). In the first scenario,  $U \gg \gamma$ , the low-energy physics near integer filling can be effectively described by a Kondo lattice model, where spin-spin interactions among local moments dominate while effectively freezing out charge fluctuations [46–50]. This scenario closely resembles the conventional Anderson lattice model, where large  $U$  strongly suppresses charge fluctuations, leaving primarily spin degrees

\* huangyi@umd.edu

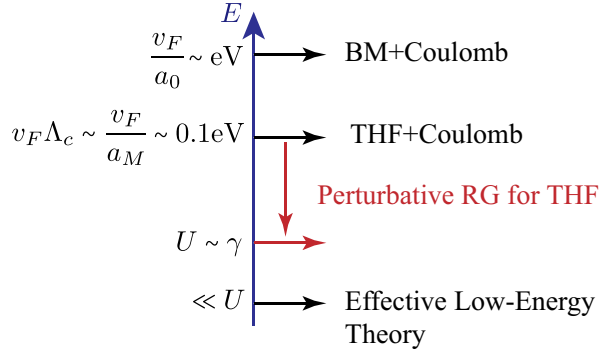


Figure 1. Energy scales of MATBG.  $v_F/a_0$  is the energy scale below which the graphene dispersion is approximated by the Dirac cone, where  $a_0$  is the graphene lattice constant.  $v_F/a_M$  characterizes the kinetic energy associated with the moiré lattice of period  $a_M$ .  $\gamma$  denotes the bandgap separating the flat bands from remote bands.  $U$  represents the Coulomb interaction strength between electrons in the flat bands.

of freedom [51]. Between integer fillings, it could be described by a mixed-valence model, analogous to Coulomb blockade physics in quantum dots, where gate voltage tuning induces significant charge fluctuations by bringing adjacent valence states closer in energy [52–54]. In contrast, the second scenario,  $U \ll \gamma$ , allows projection of remote bands out, leaving isolated flat bands that form a Mott semimetal at the charge neutrality point (CNP). Here, interactions split the initially degenerate flat bands by an energy scale of  $U$  away from the  $\Gamma_M$  point, while preserving a Dirac-like band touching at  $\Gamma_M$  due to the underlying topological structure that couples the spin and charge degrees of freedom [45, 55–57].

Practically, however, realistic ab initio calculations [34, 36, 58] and experimental observations [14, 17, 18, 33] suggest that with a lattice dielectric constant  $\kappa = 6$  and screening from double gates at a distance  $d \simeq 10$  nm, the Coulomb energy scale  $U \simeq 40$  meV is comparable to  $\gamma \simeq 30$  meV. Such an intermediate regime ( $U \sim \gamma$ ) presents considerable theoretical challenges, as it bridges the distinct conceptual limits of the  $U \gg \gamma$  and  $U \ll \gamma$  scenarios. Consequently, theoretical analyses in this intermediate regime become significantly more intricate, making it challenging to clearly identify the dominant physical picture. Performing a systematic renormalization group (RG) analysis on the parameter flow of  $U/\gamma$  within the THF model is thus highly beneficial.

In this paper, we develop a general perturbative RG framework based on the THF model to systematically analyze the flow of single-particle parameters ( $v_*$ ,  $\gamma$ ) and interaction energies ( $U$ ,  $V$ ,  $W$ ,  $J$ ,  $J_+$ ) within the energy window  $U < |E| < v_*\Lambda_c \simeq 0.1$  eV. See Fig. 1. This analysis qualitatively and quantitatively predicts how these parameters evolve. Given the practical regime  $U \sim \gamma$ , our RG approach provides valuable insights into the energy hierarchy between  $U$  and  $\gamma$  as well as the resultant low-energy physics at energies below  $U$ .

Early pioneering RG work by Vafeek and Kang (VF) [59] introduces a two-stage RG scheme that systematically integrates high-energy degrees of freedom in the BM model and

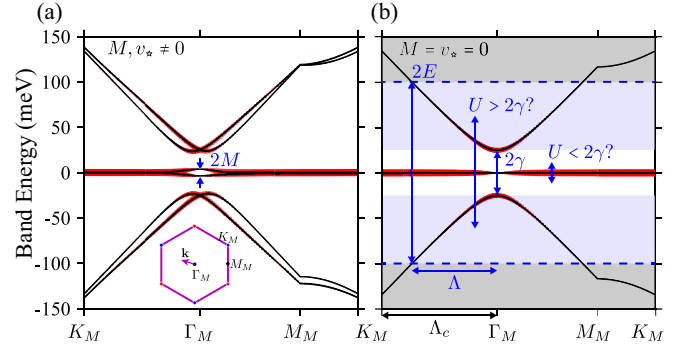


Figure 2. Band structures of the single-particle THF model fitted from the BM model with twist angle  $\theta = 1.05^\circ$  and interlayer tunneling ratio  $w_0/w_1 = 0.8$ . The model parameters are  $v_* = 4.303$  eV·Å and  $\gamma = 24.75$  meV [34]. Size of red dots represents the  $f$ -orbital weight. (a) Parameters:  $M = 3.697$  meV and  $v_* = 1.623$  eV·Å. (b)  $M = v_* = 0$ . High-energy modes above the energy cutoff  $E$  (dark shaded region) are integrated out. In our perturbative RG scheme, we continue lowering  $E$  until it reaches the bottom of the remote bands (light shaded region), where the running cutoff  $\Lambda$  flows from  $\Lambda_c$  to 0.

calculates how the parameters in the BM model such as the interlayer tunnelings  $w_0/w_1$  in the AA/AB region and graphene Dirac velocity  $v_F$  flow toward low energy. The two-stage RG are described by two energy windows,  $w_1 < |E| < v_F/a_0$  and  $|E| < w_1$ , where  $w_1 \sim 100$  meV,  $v_F/a_0 \sim 1$  eV is the graphene Dirac cone band width, and  $a_0 = 0.246$  nm is the graphene lattice constant. VK showed that Coulomb interaction suppresses the ratio  $w_0/w_1$  and drives the system toward the chiral limit ( $w_0/w_1 \rightarrow 0$ ) as the energy cutoff is lowered. Meanwhile, both  $w_1$  and  $v_F$  increase proportionally, preserving the magic-angle condition  $w_1/(v_F\Lambda_c) \simeq 1$ , where the Dirac cone displacement is given by  $\Lambda_c \sim 4\pi/3a_M$  and  $a_M = a_0/[2\sin(\theta/2)]$  is the moiré lattice constant [37]. Since  $v_*$  is of the same order as  $v_F$ , the energy window  $|E| < w_1$  in VK’s second-stage RG naturally coincides with the energy window  $|E| < v_*\Lambda_c$  in our THF-based formalism.

Unlike VK’s non-perturbative treatment of the second-stage RG—accessible only numerically—our RG analysis using the THF model remains perturbative in this same energy window and yields analytical results. Our RG results indicate that  $v_*$  and  $\gamma$  both increase by roughly a factor of 1.3, whereas  $U$  remains nearly unchanged as the energy scale is progressively reduced toward  $U$  and remote bands are integrated out (cf. Fig. 6). By comparing THF model parameters fitted from the BM model with varying  $w_0/w_1$  ratios [34, 36], we find an increase in both  $v_*$  and  $\gamma$  as the system moves toward the chiral limit ( $w_0/w_1$  decreases), consistent with VK’s findings. However, VK did not explicitly discuss the hierarchy between  $U$  and  $\gamma$ . Our RG scheme based on the THF model fills this gap by demonstrating that the ratio  $U/\gamma$  decreases as the energy cutoff is lowered. Consequently, even if the initial condition at  $|E| = v_*\Lambda_c$  satisfies  $U > \gamma$ , the projected limit  $U \ll \gamma$  near CNP can be approached under the condition  $v_*\Lambda_c/U \gg 1$ . Additionally, we compute RG flows for coupling constants associated with other interaction channels. Our analysis shows that the interaction parameters  $V$  and  $W$  exhibit minor changes

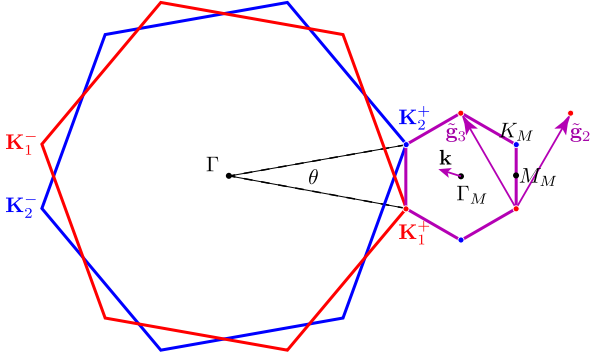


Figure 3. Brillouin zone of twisted bilayer graphene. Two graphene layers are labeled by 1 (red) and 2 (blue) with a twist  $\theta$ . The moiré Brillouin zone (purple) is shown near the graphene  $\mathbf{K}^+$  valleys, with moiré lattice vectors  $\tilde{\mathbf{g}}_2$  and  $\tilde{\mathbf{g}}_3$ .

(less than 10%), whereas the exchange interaction  $J$  increases and the double-hybridization interaction  $J_+$  decreases, resulting in an approximately twofold increase in the ratio  $J/J_+$ . These RG flows are summarized comprehensively in Fig. 7.

The structure of the paper is as follows. Section II presents the perturbative RG formalism based on the THF model, where we derive the one-loop diagrams that govern the flow equations. Section III provides the RG analysis and the corresponding main results, including the detailed derivation of the flow equations. We conclude in Section IV by summarizing our findings and discuss remaining open questions. Appendix A summarizes key integrals and identities for readers interested in technical details, and Appendix B presents all one-loop diagrams beyond the leading order and the corresponding RG equations for completeness.

## II. MODEL AND FORMALISM

In this section, we describe our perturbative RG scheme using the THF model. Our goal is to establish how the single-particle parameters ( $v_*$ ,  $\gamma$ ) and interaction strengths ( $U, V, W, J, J_+$ ) evolve under the RG flow as high-energy remote-band degrees of freedom are integrated out. To achieve this goal, we formulate the action  $S[c, f]$  including the interaction terms, and perform a momentum-shell RG by integrating out fast modes in a thin energy shell near the cutoff.

### A. THF model

We begin with the full Hamiltonian of the THF model, which describes localized  $f$ -orbitals hybridizing with dispersive  $c$ -

orbitals in the moiré lattice of MATBG [34].

$$\begin{aligned}
 H_0 = & -\mu_f \sum_{\eta, s} \sum_{\mathbf{R}} f_{\mathbf{R}, \alpha, \eta, s}^\dagger f_{\mathbf{R}, \alpha, \eta, s} + \\
 & + \sum_{\eta, s} \sum_{a, a'} \sum_{|\mathbf{k}| < \Lambda} [h_{a, a'}^{(c)\eta}(\mathbf{k}) - \mu_c \delta_{a, a'}] c_{\mathbf{k}, a, \eta, s}^\dagger c_{\mathbf{k}, a', \eta, s} + \\
 & + \frac{1}{\sqrt{N_M}} \sum_{\eta, s} \sum_{|\mathbf{k}| < \Lambda} \sum_{\mathbf{R}} \sum_{\alpha, a} [e^{i\mathbf{k} \cdot \mathbf{R}} h_{\alpha, a}^{(f)\eta}(\mathbf{k}) f_{\mathbf{R}, \alpha, \eta, s}^\dagger c_{\mathbf{k}, a, \eta, s} + h.c.]
 \end{aligned} \tag{1}$$

where  $a = 1, 2, 3, 4$  labels the  $c$ -fermions and  $\alpha = 1, 2$  labels the  $f$ -fermions.  $\eta = \pm 1$  labels the graphene  $\mathbf{K}^\pm$  valley (cf. Fig. 3), and  $s = \pm 1$  labels the spin. The Hamiltonian is defined with a momentum cutoff  $\Lambda$  that includes remote  $c$ -states beyond the first mBZ [60], as shown in Fig. 3.  $N_M$  is the total number of moiré unit cells in the finite system, which equals the number of  $\mathbf{k}$  points sampled in the first mBZ.  $\mathbf{R}$  denotes the real-space center of the  $f$  orbital in each cell. We adopt the Fourier transform of  $f$ -orbitals as follows

$$f_{\mathbf{R}, \alpha, \eta, s} = \frac{1}{\sqrt{N_M}} \sum_{\mathbf{k} \in \text{mBZ}} e^{i\mathbf{k} \cdot \mathbf{R}} f_{\mathbf{k}, \alpha, \eta, s}, \tag{2}$$

$$f_{\mathbf{k}, \alpha, \eta, s} = \frac{1}{\sqrt{N_M}} \sum_{\mathbf{R}} e^{-i\mathbf{k} \cdot \mathbf{R}} f_{\mathbf{R}, \alpha, \eta, s}. \tag{3}$$

If  $\mathbf{k}$  of an  $f$ -fermion is outside the first mBZ in Eq. (3), it should be folded back to the first mBZ denoted as  $(\mathbf{k}/\tilde{\mathbf{g}}) \in \text{mBZ}$  so that  $\mathbf{k} = m_1 \tilde{\mathbf{g}}_1 + m_2 \tilde{\mathbf{g}}_2 + \mathbf{k}/\tilde{\mathbf{g}}$ , where  $\tilde{\mathbf{g}}$  are the moiré reciprocal lattice vectors shown in Fig. 3. As a result, the non-interacting Hamiltonian can be rewritten as

$$\begin{aligned}
 H_0 = & -\mu_f \sum_{\eta, s} \sum_{\mathbf{k} \in \text{mBZ}} f_{\mathbf{k}, \alpha, \eta, s}^\dagger f_{\mathbf{k}, \alpha, \eta, s} + \\
 & + \sum_{\eta, s} \sum_{a, a'} \sum_{|\mathbf{k}| < \Lambda} [h_{a, a'}^{(c)\eta}(\mathbf{k}) - \mu_c \delta_{a, a'}] c_{\mathbf{k}, a, \eta, s}^\dagger c_{\mathbf{k}, a', \eta, s} + \\
 & + \sum_{\eta, s} \sum_{|\mathbf{k}| < \Lambda} \sum_{\alpha, a} [h_{\alpha, a}^{(f)\eta}(\mathbf{k}) f_{\mathbf{k}/\tilde{\mathbf{g}}, \alpha, \eta, s}^\dagger c_{\mathbf{k}, a, \eta, s} + h.c.],
 \end{aligned} \tag{4}$$

where the last term may describe an umklapp process that couples momentum in different mBZs when  $\Lambda$  is large compared to the first mBZ. Here, since we focus on the low-energy physics below the first remote bands, we set  $\Lambda = \Lambda_c$  and  $\Lambda_c = K_M \Gamma_M = 4\pi/3a_M$  as the first mBZ boundary (cf. Fig. 3), and we ignore the umklapp process coming from higher remote bands so that  $\mathbf{k}/\tilde{\mathbf{g}} = \mathbf{k}$  [61]. To simplify the problem further, we approximate the hexagonal first mBZ by a circle of radius  $\Lambda_c$ , so that  $\mathbf{k} \in \text{mBZ} \rightarrow |\mathbf{k}| < \Lambda_c$ . In this way, the original THF model Hamiltonian is diagonal in the momentum sector  $H_0 = \sum_{\eta, s} \sum_{|\mathbf{k}| < \Lambda_c} \Psi_{\mathbf{k}}^{\eta s \dagger} h_0^\eta(\mathbf{k}) \Psi_{\mathbf{k}}^{\eta s}$  by choosing the basis as  $\Psi = \{f_1, f_2, c_1, c_2, c_3, c_4\}$ , where we drop the valley/spin and momentum indices for simplicity. The dispersion can be solved by diagonalizing the  $6 \times 6$  Hamiltonian

$$h_0^\eta(\mathbf{k}) = \begin{bmatrix} h^{(f)\eta}(\mathbf{k}) - \mu_f & h^{(f)\eta}(\mathbf{k}) \\ h^{(cf)\eta}(\mathbf{k}) & h^{(c)\eta}(\mathbf{k}) - \mu_c \end{bmatrix}, \tag{5}$$

where  $h^{(f)\eta} = 0_{2 \times 2}$ ,

$$h^{(c)\eta} = \begin{bmatrix} 0_{2 \times 2} & v_*(\eta k_x \sigma_0 + i k_y \sigma_z) \\ v_*(\eta k_x \sigma_0 - i k_y \sigma_z) & M \sigma_x \end{bmatrix}, \tag{6}$$

and

$$h^{(fc)\eta} = h^{(cf)\eta^\dagger} = [\gamma\sigma_0 + v_*(\eta k_x\sigma_x + k_y\sigma_y), 0_{2\times 2}]. \quad (7)$$

To proceed analytically, we adopt the approximation  $M = 0$ ,  $v_* = 0$  [34], justified by the hierarchy  $M, v_*\Lambda_c \ll v_*\Lambda_c$ . Under this simplification, the non-interacting Hamiltonian  $H_0$  decouples into two independent  $3 \times 3$  blocks labeled by the orbital index  $\alpha = 1, 2$  [45]. We should emphasize that this approximation  $M = 0$ ,  $v_* = 0$  in the THF model is different from the ‘‘chiral limit’’ in the BM model where  $w_0/w_1 = 0$ . The bare parameters of the THF model at  $\Lambda_c$  are extracted using  $w_0/w_1 = 0.8$ . This simplification allows us to diagonalize  $H_0$  analytically and project the system into flat and remote band subspaces. Two decoupled sectors of the Hamiltonian formed by the basis  $\Phi_\alpha = \{f_\alpha, c_\alpha, c_{\alpha+2}\}$ ,  $\alpha = 1, 2$  are given by

$$h_0^\eta(\mathbf{k}) = h_0^{\alpha=1,\eta} \oplus h_0^{\alpha=2,\eta}, \quad (8)$$

where

$$h_0^{\eta\alpha} = \begin{bmatrix} 0 & \gamma & 0 \\ \gamma & 0 & v_*(\eta k_x + i s_\alpha k_y) \\ 0 & v_*(\eta k_x - i s_\alpha k_y) & 0 \end{bmatrix}, \quad (9)$$

$$= \begin{bmatrix} 0 & \gamma & 0 \\ \gamma & 0 & v_*|\mathbf{k}|\eta e^{i s_\alpha \eta \theta_{\mathbf{k}}} \\ 0 & v_*|\mathbf{k}|\eta e^{-i s_\alpha \eta \theta_{\mathbf{k}}} & 0 \end{bmatrix}. \quad (10)$$

Here,  $s_\alpha = (-1)^{\alpha+1}$  and  $\theta_{\mathbf{k}}$  is the angle of  $\mathbf{k}$  relative to  $\hat{k}_x$  axis. For each  $\alpha$  sector, the eigenenergies read

$$E_0 = 0, E_\pm = \pm \sqrt{v_*^2|\mathbf{k}|^2 + \gamma^2}, \quad (11)$$

and the corresponding eigenstates are given by

$$|\psi_{0,\mathbf{k}}^{\alpha\eta}\rangle = \frac{[v_*|\mathbf{k}|\eta e^{i s_\alpha \eta \theta_{\mathbf{k}}}, 0, -\gamma]^T}{\sqrt{v_*^2|\mathbf{k}|^2 + \gamma^2}}, \quad (12)$$

$$|\psi_{\pm,\mathbf{k}}^{\alpha\eta}\rangle = \frac{[\gamma\eta e^{i s_\alpha \eta \theta_{\mathbf{k}}}, \pm \eta e^{i s_\alpha \eta \theta_{\mathbf{k}}} \sqrt{v_*^2|\mathbf{k}|^2 + \gamma^2}, v_*|\mathbf{k}|]^T}{\sqrt{2(v_*^2|\mathbf{k}|^2 + \gamma^2)}}. \quad (13)$$

The Berry curvature and the resulting Chern numbers for the flat band eigenstates Eq. (12) are derived explicitly, revealing a  $U(4) \times U(4)$  symmetry due to the decomposition into  $C = \pm 1$  Chern sectors. The Berry curvature reads

$$\Omega_{\mathbf{k}}^{\alpha\eta} = \hat{z} \cdot [\nabla_{\mathbf{k}} \times \langle \psi_{0,\mathbf{k}}^{\alpha\eta} | i \nabla_{\mathbf{k}} | \psi_{0,\mathbf{k}}^{\alpha\eta} \rangle], \quad (14)$$

$$= -\frac{2v_*^2\gamma^2\eta s_\alpha}{(v_*^2|\mathbf{k}|^2 + \gamma^2)^2}, \quad (15)$$

which gives the Chern number for each flat band

$$C = \frac{1}{2\pi} \int d^2k \Omega_{\mathbf{k}}^{\alpha\eta} = -\eta s_\alpha. \quad (16)$$

We see that the whole flat-band manifold has in total 8 bands labeled by  $\alpha, \eta$ , and  $s$ , which can be decomposed into  $C = +1$  and  $C = -1$  Chern sectors where each of them has 4 bands that can be related by a  $U(4)$  rotation. As a result,  $H_0$  has  $U(4) \times U(4)$  symmetry in the limit of  $M \rightarrow 0$ ,  $v_* \rightarrow 0$  [62].

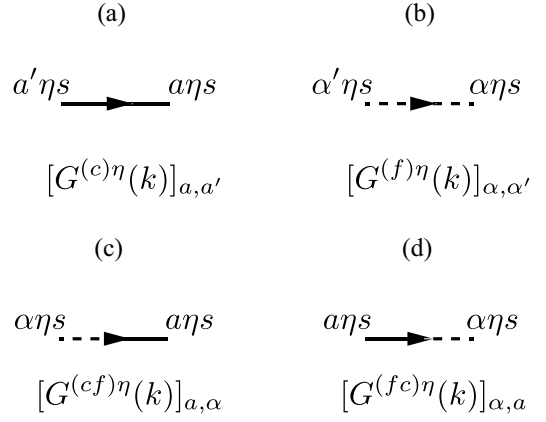


Figure 4. (a)  $c$ -fermion propagator. (b)  $f$ -fermion propagator. (c-d) Anomalous  $cf$ -propagator. The solid line represents  $c$ -fermion, and the dashed line represents  $f$ -fermion.

## B. RG formalism

We construct the imaginary-time action of the THF model defined with a momentum cutoff  $\Lambda$

$$S[c, f] = S_0[c, f] + S_I[c, f], \quad (17)$$

where  $S_0$  is non-interacting action and  $S_I$  represents the interactions. The partition function is given by

$$Z = \int \mathcal{D}[c, f] e^{-S[c, f]}. \quad (18)$$

We adopt the perturbative momentum-shell RG scheme such that we integrate out the high-energy  $c$ - and  $f$ -fermion modes in the remote bands to analyze the effective action in the low-energy regime (cf. Fig. 2 b). Focusing on CNP where  $\mu_c = \mu_f = 0$  and using the approximation  $M = v_* = 0$ ,  $S_0$  is given by

$$S_0[c, f] = \int_k \bar{\Phi}_k^{\alpha\eta s} (-i\omega \mathbb{1} + h_0^{\alpha\eta}(\mathbf{k})) \Phi_k^{\alpha\eta s}, \quad (19)$$

where we use Einstein’s summation convention to sum over the dummy indices and integrate over  $k = \{\omega, \mathbf{k}\}$ , the Matsubara frequency  $\omega$  and momentum  $\mathbf{k}$ ,

$$\int_k = \int_{-\infty}^{\infty} \frac{d\omega}{2\pi} \int \frac{d^2\mathbf{k}}{(2\pi)^2} \Theta(\Lambda - |\mathbf{k}|). \quad (20)$$

The band basis  $\{\bar{\Phi}_k^{\alpha\eta s}\}$  is defined as

$$\Phi_k^{\alpha\eta s} = [f_{k,\alpha,\eta,s}, c_{k,\alpha,\eta,s}, c_{k,\alpha+2,\eta,s}]^T, \quad (21)$$

$$\bar{\Phi}_k^{\alpha\eta s} = [\bar{f}_{k,\alpha,\eta,s}, \bar{c}_{k,\alpha,\eta,s}, \bar{c}_{k,\alpha+2,\eta,s}]. \quad (22)$$

The non-interacting action can be projected onto the flat bands and remote bands by a change of basis  $\{\bar{\psi}_{b,k}^{\alpha\eta s} = \bar{\Phi}_k^{\alpha\eta s} |\psi_{b,k}^{\alpha\eta}\rangle\}$  where  $b = 0, \pm$ ,

$$S_0[c, f] = S_{0,0}[\psi_0] + S_{0,1}[\psi_\pm], \quad (23)$$

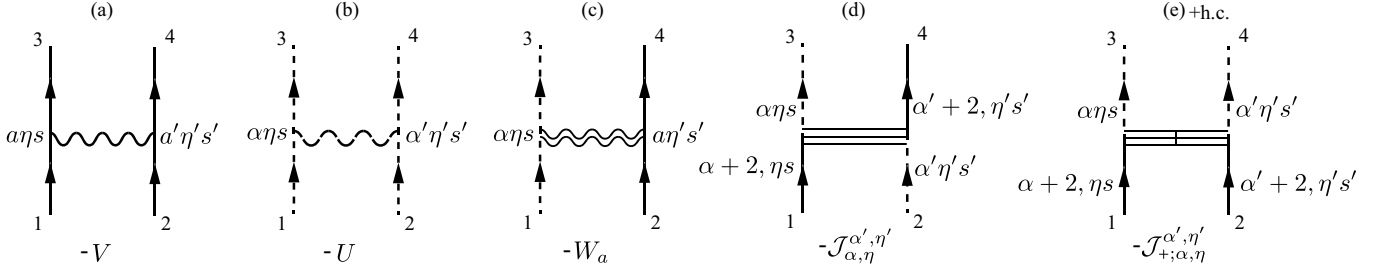


Figure 5. Coulomb interactions between  $c$ - and  $f$ -fermions.  $c$ -fermion ( $f$ -fermion) is denoted as a solid (dashed) line with an arrow. Due to symmetry,  $W_1 = W_2$ ,  $W_3 = W_4$ .  $\mathcal{J}_{\alpha,\eta}^{\alpha',\eta'} = J(\eta\eta' + s_\alpha s_{\alpha'})/2$  and  $\mathcal{J}_{+;\alpha,\eta}^{\alpha',\eta'} = -J_+(\eta\eta' - s_\alpha s_{\alpha'})/2$  where  $s_\alpha = (-)^{\alpha-1}$ .

where the projected actions read

$$\begin{aligned} S_{0,0} &= \int_k \bar{\Phi}_k^{\alpha\eta s} P_0 (-i\omega \mathbb{1} + h_0^{\alpha\eta}(\mathbf{k})) P_0 \Phi_k^{\alpha\eta s}, \\ &= \int_k \bar{\psi}_{0,k}^{\alpha\eta s} (-i\omega \mathbb{1} + E_0) \psi_{0,k}^{\alpha\eta s}, \end{aligned} \quad (24)$$

$$\begin{aligned} S_{0,1} &= \int_k \bar{\Phi}_k^{\alpha\eta s} P_1 (-i\omega \mathbb{1} + h_0^{\alpha\eta}(\mathbf{k})) P_1 \Phi_k^{\alpha\eta s}, \\ &= \int_k \sum_{b=\pm} \bar{\psi}_{b,k}^{\alpha\eta s} (-i\omega \mathbb{1} + E_b(\mathbf{k})) \psi_{b,k}^{\alpha\eta s}. \end{aligned} \quad (25)$$

Here,  $P_0 = |\psi_{0,\mathbf{k}}^{\alpha\eta}\rangle\langle\psi_{0,\mathbf{k}}^{\alpha\eta}|$  and  $P_1 = \sum_{b=\pm} |\psi_{b,\mathbf{k}}^{\alpha\eta}\rangle\langle\psi_{b,\mathbf{k}}^{\alpha\eta}| = \mathbb{1} - P_0$  are the corresponding projection operators to the flat bands and remote bands, respectively. The non-interacting Green function  $G^{\alpha\eta}(k) = (i\omega \mathbb{1} - h_0^{\alpha\eta}(\mathbf{k}))^{-1}$  reads

$$\begin{aligned} G^{\alpha\eta}(z = i\omega, \mathbf{k}) &= \sum_{b=0,\pm} \frac{|\psi_{b,\mathbf{k}}^{\alpha\eta}\rangle\langle\psi_{b,\mathbf{k}}^{\alpha\eta}|}{z - E_b}, \\ &= G_0^{\alpha\eta}(z, \mathbf{k}) + G_1^{\alpha\eta}(z, \mathbf{k}), \end{aligned} \quad (26)$$

where  $G_0$  and  $G_1$  are Green functions projected to the flat bands and the remote bands, respectively:

$$\begin{aligned} G_0^{\alpha\eta}(z = i\omega, \mathbf{k}) &= \frac{|\psi_{0,\mathbf{k}}^{\alpha\eta}\rangle\langle\psi_{0,\mathbf{k}}^{\alpha\eta}|}{z - E_0} = \frac{1}{z(v_*^2|\mathbf{k}|^2 + \gamma^2)} \times \\ &\times \begin{bmatrix} v_*^2|\mathbf{k}|^2 & 0 & -\gamma v_* |\mathbf{k}| \eta e^{i s_\alpha \eta \theta_{\mathbf{k}}} \\ 0 & 0 & 0 \\ -\gamma v_* |\mathbf{k}| \eta e^{-i s_\alpha \eta \theta_{\mathbf{k}}} & 0 & \gamma^2 \end{bmatrix}, \end{aligned} \quad (27)$$

$$\begin{aligned} G_1^{\alpha\eta}(z = i\omega, \mathbf{k}) &= \sum_{b=\pm} \frac{|\psi_{b,\mathbf{k}}^{\alpha\eta}\rangle\langle\psi_{b,\mathbf{k}}^{\alpha\eta}|}{z - E_b} = \frac{-1}{-z^2 + v_*^2|\mathbf{k}|^2 + \gamma^2} \times \\ &\times \begin{bmatrix} \frac{z\gamma^2}{v_*^2|\mathbf{k}|^2 + \gamma^2} & \gamma & \frac{z\gamma v_* |\mathbf{k}| \eta e^{i s_\alpha \eta \theta_{\mathbf{k}}}}{v_*^2|\mathbf{k}|^2 + \gamma^2} \\ \gamma & z & v_* |\mathbf{k}| \eta e^{i s_\alpha \eta \theta_{\mathbf{k}}} \\ \frac{z\gamma v_* |\mathbf{k}| \eta e^{-i s_\alpha \eta \theta_{\mathbf{k}}}}{v_*^2|\mathbf{k}|^2 + \gamma^2} & v_* |\mathbf{k}| \eta e^{-i s_\alpha \eta \theta_{\mathbf{k}}} & \frac{z v_*^2 |\mathbf{k}|^2}{v_*^2|\mathbf{k}|^2 + \gamma^2} \end{bmatrix}, \\ &= \begin{bmatrix} G^{(f)\eta} & G^{(fc)\eta} \\ G^{(cf)\eta} & G^{(c)\eta} \end{bmatrix}. \end{aligned} \quad (28)$$

Since we only integrate out the remote bands in our RG scheme, we focus on the remote band Green function Eq. (28) whose

diagrams are shown in Fig. 4. We divide the remote-band fermion modes into two parts, the slow modes  $\psi_{\pm,k}^<$  with  $|\mathbf{k}| < \Lambda - d\Lambda$  and the fast modes  $\psi_{\pm,k}^>$  within a momentum shell  $\Lambda - d\Lambda < |\mathbf{k}| < \Lambda$ . To relate the fermionic operators in the eigenbasis to those in the band basis, we use the notation  $\hat{O}[c_k^<, f_k^<] \equiv \hat{O}[\psi_{0,k}, \psi_{\pm,k}^<]$  and  $\hat{O}[c_k^>, f_k^>] \equiv \hat{O}[\psi_{\pm,k}^>]$ . This notation indicates that these are the same fermionic operators  $\hat{O}$ , expressed in different bases. In particular, the Jacobian of this basis transformation in the path integral equals the identity. The perturbative RG is performed by integrating the high-energy remote-band fermions  $\psi_{\pm,k}^>$ , while retaining the flat-band  $\psi_0$  and low-energy remote-band modes  $\psi_{\pm,k}^<$ . The partition function can be rewritten as

$$\begin{aligned} Z &= \int \mathcal{D}[\psi_0, \psi_{\pm}^<] e^{-S_{0,0}[\psi_0] - S_{0,1}[\psi_{\pm}^<]} \times \\ &\times \int \mathcal{D}[\psi_{\pm}^>] e^{-S_{0,1}[\psi_{\pm}^>] - S_I[c, f]}, \end{aligned} \quad (29)$$

$$= \int \mathcal{D}[\psi_0, \psi_{\pm}^<] e^{-S_{\text{eff}}[\psi_0, \psi_{\pm}^<]}, \quad (30)$$

where the effective action is given by

$$S_{\text{eff}} = S_{0,0}[\psi_0] + S_{0,1}[\psi_{\pm}^<] - \ln Z_{0,1}^> - \ln[\langle e^{-S_I} \rangle]. \quad (31)$$

We introduce the partial trace over  $\psi_{\pm}^>$  fields

$$\langle \hat{O} \rangle = \frac{1}{Z_{0,1}^>} \int \mathcal{D}[\psi_{\pm}^>] e^{-S_{0,1}[\psi_{\pm}^>]} \hat{O}[c, f], \quad (32)$$

$$= \frac{1}{Z_{0,1}^>} \int \mathcal{D}[c^>, f^>] e^{-S_{0,1}[c^>, f^>]} \hat{O}[c, f]. \quad (33)$$

Here,  $Z_{0,1}^> = \int \mathcal{D}[\psi_{\pm}^>] e^{-S_{0,1}[\psi_{\pm}^>]}$  is the partition function for the fermion modes in the momentum shell of the remote bands, which is a normalization factor of the partial trace. The non-interacting remote-band Green function Eq. (28) (cf. Fig. 4) can be rewritten using this partial trace notation

$$[G^{(c)\eta}(k)]_{a,a'} = -\langle c_{k,a,\eta,s} \bar{c}_{k,a',\eta,s} \rangle, \quad (34)$$

$$[G^{(f)\eta}(k)]_{\alpha,\alpha'} = -\langle f_{k,\alpha,\eta,s} \bar{f}_{k,\alpha',\eta,s} \rangle, \quad (35)$$

$$[G^{(cf)\eta}(k)]_{a,\alpha} = -\langle c_{k,a,\eta,s} \bar{f}_{k,\alpha,\eta,s} \rangle, \quad (36)$$

$$[G^{(fc)\eta}(k)]_{\alpha,a} = -\langle f_{k,\alpha,\eta,s} \bar{c}_{k,a,\eta,s} \rangle. \quad (37)$$

$\frac{\mathcal{J}_{\alpha,\eta}^{\alpha',\eta'}}{J} \Big _{\eta=\eta'} \Big _{\eta \neq \eta'}$	$\frac{\mathcal{J}_{+;\alpha,\eta}^{\alpha',\eta'}}{J_+} \Big _{\eta=\eta'} \Big _{\eta \neq \eta'}$
$\alpha = \alpha'$ +    0	$\alpha = \alpha'$ 0    +
$\alpha \neq \alpha'$ 0    -	$\alpha \neq \alpha'$ -    0

Table I. Valley-orbital texture of exchange and double-hybridization interaction. Left:  $\mathcal{J}_{\alpha,\eta}^{\alpha',\eta'} = J(\eta\eta' + s_\alpha s_{\alpha'})/2$ ; Right:  $\mathcal{J}_{+;\alpha,\eta}^{\alpha',\eta'} = -J_+(\eta\eta' - s_\alpha s_{\alpha'})/2$ . Here,  $\eta, \eta' \in \{+, -\}$ ,  $\alpha, \alpha' \in \{1, 2\}$ , and  $s_\alpha = (-)^{\alpha-1}$ .

The Coulomb interaction projected on the band basis reads

$$S_U = \frac{U}{2} \int_{\{k_i\}} \bar{f}_{k_3,\alpha,\eta,s} \bar{f}_{k_4,\alpha',\eta',s} f_{k_2,\alpha',\eta',s'} f_{k_1,\alpha,\eta,s}, \quad (38)$$

$$S_V = \frac{V}{2} \int_{\{k_i\}} \bar{c}_{k_3,a,\eta,s} \bar{c}_{k_4,a',\eta',s} c_{k_2,a',\eta',s'} c_{k_1,a,\eta,s}, \quad (39)$$

$$S_W = W_\alpha \int_{\{k_i\}} \bar{f}_{k_3,\alpha,\eta,s} \bar{c}_{k_4,a,\eta',s'} c_{k_2,a,\eta',s'} f_{k_1,\alpha,\eta,s}, \quad (40)$$

$$S_J = \mathcal{J}_{\alpha,\eta}^{\alpha',\eta'} \times \int_{\{k_i\}} \bar{f}_{k_3,\alpha,\eta,s} \bar{c}_{k_4,\alpha'+2,\eta',s'} f_{k_2,\alpha',\eta',s'} c_{k_1,\alpha+2,\eta,s}, \quad (41)$$

$$S_{J_+} = \frac{1}{2} \mathcal{J}_{+;\alpha,\eta}^{\alpha',\eta'} \times \int_{\{k_i\}} (\bar{f}_{k_3,\alpha,\eta,s} \bar{f}_{k_4,\alpha',\eta',s'} c_{k_2,\alpha'+2,\eta',s'} c_{k_1,\alpha+2,\eta,s} + \text{h.c.}), \quad (42)$$

where  $\mathcal{J}_{\alpha,\eta}^{\alpha',\eta'} = J(\eta\eta' + s_\alpha s_{\alpha'})/2$  and  $\mathcal{J}_{+;\alpha,\eta}^{\alpha',\eta'} = -J_+(\eta\eta' - s_\alpha s_{\alpha'})/2$ , and we use the integral notation

$$\int_{\{k_i\}} = \int_{\{|\mathbf{k}_i| < \Lambda\}} \prod_{i=1}^4 \left[ \frac{d^2 \mathbf{k}_i d\omega_i}{(2\pi)^3} \right] \times (2\pi)^3 \delta(\mathbf{k}_1 + \mathbf{k}_2 - \mathbf{k}_3 - \mathbf{k}_4) \delta(\omega_1 + \omega_2 - \omega_3 - \omega_4). \quad (43)$$

Since the non-interacting action  $S_0$  (in the limit of  $M, v_* \rightarrow 0$ ) and the interaction terms  $S_U, S_V, S_W, S_J, S_{J_+}$  all have the  $U(4) \times U(4)$  symmetry, the full interacting MATBG system also preserves this symmetry [34]. Here, the matrix elements in  $J$  and  $J_+$  terms enforce certain textures in the valley ( $\eta, \eta'$ ) and orbital ( $\alpha, \alpha'$ ) indices between two interacting electrons. See Table I. These interactions are represented diagrammatically in Fig. 5. The interaction terms can be evaluated perturbatively through cumulant expansion

$$\ln[\langle e^{-S_I} \rangle] = -\langle S_I \rangle + \frac{1}{2} (\langle S_I^2 \rangle - \langle S_I \rangle^2) + \dots + \frac{(-)^l}{l!} \times l\text{-th cumulant of } S_I + \dots \quad (44)$$

As a result, the one-loop perturbative correction to the interaction can be obtained through

$$\delta S_I = -\ln[\langle e^{-S_I} \rangle] \approx \langle S_I \rangle - \frac{1}{2} (\langle S_I^2 \rangle - \langle S_I \rangle^2). \quad (45)$$

The first-order term  $\delta S_I^{(1)} = \langle S_I \rangle$  yields the flow equations for  $v_*$  and  $\gamma$  [cf. the self-energy diagrams shown in Fig. 8 and Eqs. (46-47)]. The second-order term  $\delta S_I^{(2)} = -\frac{1}{2} (\langle S_I^2 \rangle - \langle S_I \rangle^2)$  generate the RG flow for  $U, V, W, J, J_+$  [cf. the leading one-loop vertex corrections shown in Fig. 9 and Eqs. (48-53)].

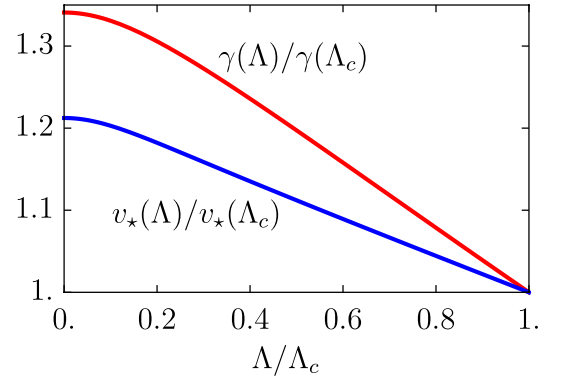


Figure 6. RG flow of  $\gamma$  and  $v_*$ . The initial conditions at  $\Lambda_c$  are  $v_* = 4.303 \text{ eV}\cdot\text{\AA}$ ,  $\gamma = 24.75 \text{ meV}$ ,  $V = 48.31 \text{ meV}$ ,  $U = 57.95 \text{ meV}$ ,  $W_1 = 44.03 \text{ meV}$ ,  $W_3 = 50.20 \text{ meV}$ ,  $J = J_+ = 16.38 \text{ meV}$ .

### III. RG ANALYSIS AND MAIN RESULTS

We now present and derive the main results of our perturbative RG analysis for the THF model of MATBG [34]. Our analysis reveals how both single-particle parameters and interaction strengths evolve as high-energy remote-band degrees of freedom are systematically integrated out, providing a self-consistent route to low-energy effective theory near charge neutrality. The central findings are summarized in Figs. 6 and 7 and Eqs. (46-53), which show the RG flow of the hybridization strength  $\gamma$ , the  $c$ -fermion velocity  $v_*$ , and various interaction couplings  $V, U, W, J$ , and  $J_+$ . In the rest of the section, we discuss these main results and provide details of the derivations.

#### A. RG differential equations

With the formalism discussed in the previous section, we analytically derive the leading order one-loop RG equations by integrating out the remote bands. The one-loop RG equations for  $v_*$  and  $\gamma$  are:

$$\frac{d \ln |v_*|}{d\Lambda} = -V \frac{1}{8\pi} \frac{(v_*^2 \Lambda^2 + 2\gamma^2) \Lambda}{(v_*^2 \Lambda^2 + \gamma^2)^{3/2}}, \quad (46)$$

$$\frac{d \ln |\gamma|}{d\Lambda} = -W_1 \frac{1}{4\pi} \frac{\Lambda}{(v_*^2 \Lambda^2 + \gamma^2)^{1/2}}. \quad (47)$$

The results show that both  $v_*$  and  $\gamma$  increase as  $\Lambda$  decreases under RG. The RG equations for the interaction couplings (to

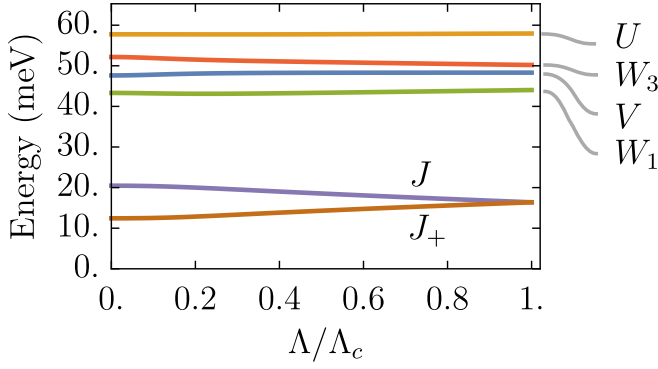


Figure 7. RG flow of interactions. The initial conditions at  $\Lambda_c$  are  $v_* = 4.303 \text{ eV}\cdot\text{\AA}$ ,  $\gamma = 24.75 \text{ meV}$ ,  $V = 48.31 \text{ meV}$ ,  $U = 57.95 \text{ meV}$ ,  $W_1 = 44.03 \text{ meV}$ ,  $W_3 = 50.20 \text{ meV}$ ,  $J = J_+ = 16.38 \text{ meV}$ .

leading order) are:

$$\frac{dV}{d\Lambda} = \mathcal{O}\left(\frac{\gamma^4}{v_*^4 \Lambda^4}\right), \quad (48)$$

$$\frac{dU}{d\Lambda} = \frac{[(W_1 - W_3)^2 + \frac{1}{4}J(W_1 - W_3)]}{\pi v_*} + \mathcal{O}\left(\frac{\gamma^2}{v_*^2 \Lambda^2}\right), \quad (49)$$

$$\frac{dW_1}{d\Lambda} = -\frac{1}{8\pi v_*} V(W_1 - W_3) + \mathcal{O}\left(\frac{\gamma^2}{v_*^2 \Lambda^2}\right), \quad (50)$$

$$\frac{dW_3}{d\Lambda} = \frac{1}{8\pi v_*} V(W_1 - W_3) + \mathcal{O}\left(\frac{\gamma^2}{v_*^2 \Lambda^2}\right), \quad (51)$$

$$\frac{dJ}{d\Lambda} = -\frac{1}{8\pi v_*} VJ + \mathcal{O}\left(\frac{\gamma^2}{v_*^2 \Lambda^2}\right), \quad (52)$$

$$\frac{dJ_+}{d\Lambda} = \frac{1}{8\pi v_*} VJ_+ + \mathcal{O}\left(\frac{\gamma^2}{v_*^2 \Lambda^2}\right). \quad (53)$$

The detailed derivation of the RG Eqs. (46-53) are given in Sec. III B, and the full RG equations including all subleading one-loop contributions are given in Appendix B. Here, the interaction strengths  $V, U, W, J, J_+$  are in units of  $\text{meV}\cdot\Omega_0$ , where  $\Omega_0 = a_M^2 \sqrt{3}/2$  represents the area of a moiré unit cell,  $a_M = 13.4 \text{ nm}$  is the moiré lattice constant at the magic angle  $\theta = 1.05^\circ$ . For convenience, we set  $\Omega_0 \rightarrow 1$  in the RG equations and the corresponding RG flow plots in Figs. 6 and 7.  $\Lambda$  labels the momentum of remote band electrons, above which we integrate out in the partition function. The (ultraviolet) initial conditions at  $\Lambda_c = 4\pi/3a_M$  for the single-particle parameters and interaction strengths are chosen to match the THF model corresponding to  $w_0/w_1 = 0.8$  and  $\theta = 1.05^\circ$  with projected Coulomb interaction screened by a dual gate separated by 10 nm hBN from the MATBG and a lattice dielectric constant  $\kappa = 6$  [34]. The initial values at  $\Lambda_c$  are  $v_* = 4.303 \text{ eV}\cdot\text{\AA}$ ,  $\gamma = 24.75 \text{ meV}$ ,  $V = 48.31 \text{ meV}$ ,  $U = 57.95 \text{ meV}$ ,  $W_1 = 44.03 \text{ meV}$ ,  $W_3 = 50.20 \text{ meV}$ ,  $J = J_+ = 16.38 \text{ meV}$  [34]. For systems with different  $\theta$ ,  $w_0/w_1$ , and  $d$ , the initial interaction values at the cutoff  $\Lambda_c$  should be adjusted accordingly, as discussed in Ref. [36].

Numerical integration of these equations, using parameters fitted from the BM model with  $w_0/w_1 = 0.8$  and  $\theta = 1.05^\circ$ ,

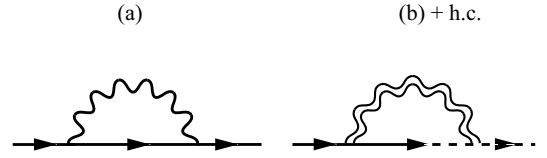


Figure 8. Leading non-zero self-energy correction.

shows that  $v_*$  and  $\gamma$  increase by approximately 30% over the RG flow window (see Fig. 6). Importantly, this RG flow in the THF model is consistent with the trend toward the chiral limit in the BM model [59], where the AA/AB tunneling ratio  $w_0/w_1$  decreases. Fitting (non-interacting) THF model parameters from BM calculations with varying  $w_0/w_1$  confirms that both  $v_*$  and  $\gamma$  increase as  $w_0/w_1$  is lowered (see, e.g., Table S4 in Ref. [34] and Table S38 in Ref. [36]), consistent with the upward flow observed in our RG treatment. We emphasize that this tendency to approach the chiral limit of the BM model is not an artifact of setting  $M$  and  $v_*$  to zero.

On the other hand, for the interaction strengths, we observe the following qualitative trends (see Fig. 7).  $U$  remains nearly constant throughout the RG flow, validating the use of its UV values for low-energy modeling [34, 36, 45–50, 56, 58].  $V$  and  $W$  also experience only weak renormalization (on the order of 10%). On the other hand,  $J$  increases while  $J_+$  decreases, leading to a roughly doubling of the ratio  $J/J_+$  in the flow window. This reflects the enhanced importance of exchange interactions over double-hybridization-assisted processes in the low-energy effective Hamiltonian.

Since  $\gamma$  increases while  $U$  remains nearly unchanged under RG, this flow leads to a decreasing ratio  $U/\gamma$  as the cutoff  $\Lambda$  is lowered. Theoretically, in the limit of  $v_* \Lambda_c \gg U, \gamma$ , this RG flow effectively drives the system towards the projected-limit/Mott-semimetal regime where  $U \ll \gamma$ , even given  $U > \gamma$  at the UV scale. In practice, the ratios  $v_* \Lambda_c / U \sim 3$  and  $v_* \Lambda_c / \gamma \sim 5$  are finite, so the resulting energy hierarchy depends on the initial conditions. However, the trend that  $U/\gamma$  decreases under RG still holds.

## B. Derivation of Flow Equations

Here, we compute the one-loop diagrams shown in Fig. 9-11 and derive our results of RG flows given by Eqs. (46-53). Throughout the calculation, we take the external momenta to be small compared to internal momenta in the shell, a standard approximation in momentum-shell RG, since we are interested in the low-energy physics. For example, when we compute the exchange self-energy, we are going to evaluate integral such as

$$\int' \frac{d^2 \mathbf{q}}{(2\pi)^2} \int_{-\infty}^{\infty} \frac{d\nu}{2\pi} G_1^{\alpha\eta}(i\omega + i\nu, \mathbf{k} + \mathbf{q}), \quad (54)$$

where  $\{\omega, \mathbf{k}\}$  are external and  $\{\nu, \mathbf{q}\}$  are internal, and  $\int'$  indicates the integral range is over the momentum shell  $\Lambda - d\Lambda < |\mathbf{q}| < \Lambda$ . On the other hand, the bubble self-energy diagrams involve integral  $\int'_q G_1^{\alpha\eta}(q)$ , which vanishes except the matrix

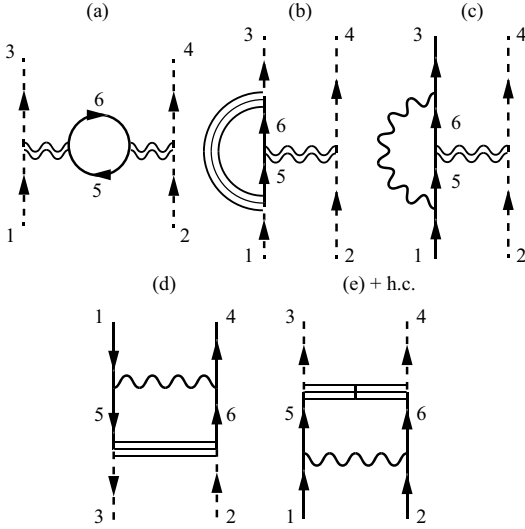


Figure 9. Leading non-zero one-loop diagrams for interaction correction.

element between  $f_\alpha$  and  $c_\alpha$ :

$$\int_q' G_1^{\alpha\eta}(q) = -\frac{\Lambda d\Lambda}{4\pi\sqrt{v_*^2\Lambda^2 + \gamma^2}} \begin{bmatrix} 0 & \gamma & 0 \\ \gamma & 0 & 0 \\ 0 & 0 & 0 \end{bmatrix}. \quad (55)$$

However, for the interactions Eqs. (38-42) [cf. Fig. 5], there is no vertex connecting  $f_\alpha$  and  $c_\alpha$ , so there is no bubble self-energy correction. Note that the interactions  $J$  and  $J_+$  [Eqs. (41-42)] involve  $f_\alpha$  and  $c_{\alpha+2}$  (not  $c_\alpha$ ). To compute the exchange integral, Eq. (54), one can expand the Green function  $G_1(k+q)$  to the leading order in  $k$  assuming  $k \ll q$ :

$$G_1^{\alpha\eta}(z+x, \mathbf{k}+\mathbf{q}) \approx G_1^{\alpha\eta}(x, \mathbf{q}) + \delta G^{\alpha\eta}(x, \mathbf{q}; z, \mathbf{k}). \quad (56)$$

The full expressions of  $\delta G$  and the corresponding integrals are shown in Appendix A. This leads to

$$\int_q' \delta G^{\alpha\eta}(q, k) \approx -\frac{\Lambda d\Lambda}{8\pi} \frac{(v_*^2\Lambda^2 + 2\gamma^2)}{(v_*^2\Lambda^2 + \gamma^2)^{3/2}} \times \begin{bmatrix} 0 & 0 & 0 \\ 0 & 0 & v_*|\mathbf{k}|\eta e^{i\eta s_\alpha \theta_{\mathbf{k}}} \\ 0 & v_*|\mathbf{k}|\eta e^{-i\eta s_\alpha \theta_{\mathbf{k}}} & 0 \end{bmatrix}. \quad (57)$$

As a result, only the exchange diagrams in Fig. 8 have non-zero contribution. The exchange diagram in Fig. 8 (a) reads

$$\delta S_{(a)}^{(1)} = -\int_k \bar{c}_{k,a,\eta,s} c_{k,a',\eta,s} \int_q' V G_{a,a'}^{(c)\eta}(k+q), \quad (58)$$

$$\approx -\int_k \bar{c}_{k,a,\eta,s} c_{k,a',\eta,s} \int_q' V \delta G_{a,a'}^{(c)\eta}(q, k), \quad (59)$$

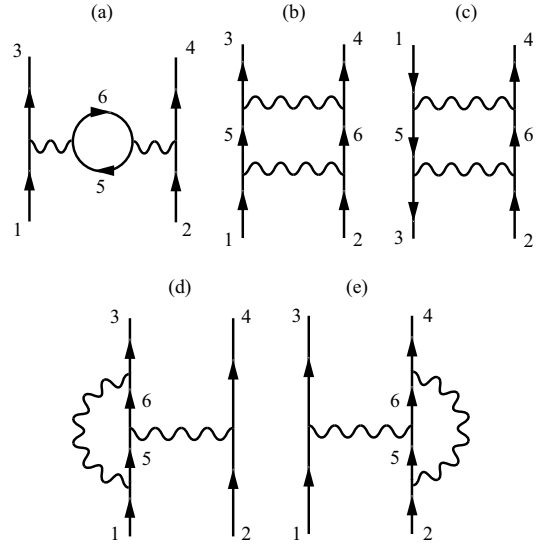


Figure 10.  $c$ -fermion (or  $V$ ) only one-loop diagram.

which contributes to the renormalization of  $c$ -fermion velocity  $v_*$  [cf. Eqs. (46, 57)]:

$$\begin{aligned} \delta v_* &= v_*(\Lambda - d\Lambda) - v_*(\Lambda), \\ &= \int' \frac{d^2\mathbf{q}}{(2\pi)^2} \int_{-\infty}^{\infty} \frac{d\nu}{2\pi} \frac{(\nu^2 + \gamma^2)v_*}{(\nu^2 + v_*^2|\mathbf{q}|^2 + \gamma^2)}, \\ &= v_* \frac{V}{8\pi} \frac{(v_*^2\Lambda^2 + 2\gamma^2)\Lambda d\Lambda}{(v_*^2\Lambda^2 + \gamma^2)^{3/2}}. \end{aligned} \quad (60)$$

Similarly, the exchange diagram in Fig. 8 (b) reads

$$\delta S_{(b)}^{(1)} = -\int_k \bar{f}_{k,\alpha,\eta,s} c_{k,a,\eta,s} \int_q' W_a G_{\alpha,a}^{(fc)\eta}(k+q), \quad (61)$$

$$\approx -\int_k \bar{f}_{k,\alpha,\eta,s} c_{k,a,\eta,s} \int_q' W_a G_{\alpha,a}^{(fc)\eta}(q), \quad (62)$$

which contributes to the renormalization of  $\gamma$  [cf. Eqs. (47, 55-57)]:

$$\begin{aligned} \delta\gamma &= \gamma(\Lambda - d\Lambda) - \gamma(\Lambda) = -\int_q' W_a G_{\alpha,a}^{(fc)\eta}(q), \\ &= \int' \frac{d^2\mathbf{q}}{(2\pi)^2} \int_{-\infty}^{\infty} \frac{d\nu}{2\pi} \frac{\delta_{\alpha,a} W_1 \gamma}{\nu^2 + v_*^2|\mathbf{q}|^2 + \gamma^2}, \\ &= \gamma \frac{W_1}{4\pi} \frac{\Lambda d\Lambda}{(v_*^2\Lambda^2 + \gamma^2)^{1/2}}. \end{aligned} \quad (63)$$

Next, we compute the leading one-loop diagrams for interactions shown in Figs. 9 and 10 by treating  $\gamma/(v_*\Lambda)$  as a small parameter. By setting the external momentum to zero, we have

the diagrams in Fig. 9

$$\delta S_{(a)}^{(2)} \approx \frac{1}{2} \int_{\{k_i\}} \bar{f}_{k_3, \alpha, \eta, s} \bar{f}_{k_4, \alpha', \eta', s'} f_{k_2, \alpha', \eta', s'} f_{k_1, \alpha, \eta, s} \times \int_q' \sum_{\eta, s, a_1, a_2} G_{a_1, a_2}^{(c)\eta}(q) G_{a_2, a_1}^{(c)\eta}(q) W_{a_1} W_{a_2}, \quad (64)$$

$$\delta S_{(b)}^{(2)} \approx -\frac{1}{2} \times 2 \int_{\{k_i\}} \bar{f}_{k_3, \alpha, \eta, s} \bar{f}_{k_4, \alpha', \eta', s'} f_{k_2, \alpha', \eta', s'} f_{k_1, \alpha, \eta, s} \times \int_q' \sum_a G_{a, \alpha'+2}^{(c)\eta}(q) G_{\alpha'+2, a}^{(c)\eta}(q) W_a J, \quad (65)$$

$$\delta S_{(c)}^{(2)} \approx -\frac{1}{2} \times 2 \int_{\{k_i\}} \bar{c}_{k_3, a, \eta, s} \bar{f}_{k_4, \alpha, \eta', s'} f_{k_2, \alpha, \eta', s'} c_{k_1, a, \eta, s} \times \int_q' \sum_{a_1} G_{a_1, a}^{(c)\eta}(q) G_{a, a_1}^{(c)\eta}(q) V W_{a_1}, \quad (66)$$

$$\delta S_{(d)}^{(2)} \approx -\frac{1}{2} \times 2 \int_{\{k_i\}} \bar{f}_{k_3, \alpha, \eta, s} \bar{c}_{k_4, a', \eta', s'} f_{k_2, \alpha', \eta', s'} c_{k_1, a, \eta, s} \times \int_q' G_{\alpha+2, a}^{(c)\eta}(q) G_{a', \alpha'+2}^{(c)\eta'}(q) V J \frac{1}{2} (\eta \eta' + s_\alpha s_{\alpha'}), \quad (67)$$

$$\delta S_{(e)}^{(2)} \approx -\frac{1}{2} \times 2 \int_{\{k_i\}} \bar{f}_{k_3, \alpha, \eta, s} \bar{f}_{k_4, \alpha', \eta', s'} c_{k_2, a', \eta', s'} c_{k_1, a, \eta, s} \times \int_q' G_{\alpha+2, a}^{(c)\eta}(q) G_{\alpha'+2, a'}^{(c)\eta'}(-q) V (-J_+) \frac{1}{2} (\eta \eta' - s_\alpha s_{\alpha'}), \quad (68)$$

which corresponds to the following interaction correction

$$\delta U^{(a)} = 8 \int' \frac{d^2 \mathbf{q}}{(2\pi)^2} \int_{-\infty}^{\infty} \frac{d\nu}{2\pi} \times \frac{2v_*^2 |\mathbf{q}|^2 W_1 W_3 - \nu^2 W_1^2 - \frac{\nu^2 v_*^4 |\mathbf{q}|^4 W_3^2}{(v_*^2 |\mathbf{q}|^2 + \gamma^2)^2}}{(\nu^2 + v_*^2 |\mathbf{q}|^2 + \gamma^2)^2}, \quad (69)$$

$$= -\frac{1}{\pi} \Lambda d\Lambda \frac{[v_*^2 \Lambda^2 (W_1 - W_3) + W_1 \gamma^2]^2}{(v_*^2 \Lambda^2 + \gamma^2)^{5/2}},$$

$$\delta U^{(b)} = \int' \frac{d^2 \mathbf{q}}{(2\pi)^2} \int_{-\infty}^{\infty} \frac{d\nu}{2\pi} J \frac{v_*^2 |\mathbf{q}|^2 \left( W_1 - \frac{\nu^2 v_*^2 |\mathbf{q}|^2 W_3}{(v_*^2 |\mathbf{q}|^2 + \gamma^2)^2} \right)}{(\nu^2 + v_*^2 |\mathbf{q}|^2 + \gamma^2)^2} \quad (70)$$

$$= -J \frac{1}{4\pi} \Lambda d\Lambda \frac{v_*^2 \Lambda^2 [v_*^2 \Lambda^2 (W_1 - W_3) + W_1 \gamma^2]}{(v_*^2 \Lambda^2 + \gamma^2)^{5/2}},$$

$$\delta W_1^{(c)} = V \int' \frac{d^2 \mathbf{q}}{(2\pi)^2} \int_{-\infty}^{\infty} \frac{d\nu}{2\pi} \frac{v_*^2 |\mathbf{q}|^2 W_3 - \nu^2 W_1}{(\nu^2 + v_*^2 |\mathbf{q}|^2 + \gamma^2)^2}, \quad (71)$$

$$= V \frac{1}{8\pi} \Lambda d\Lambda \frac{v_*^2 \Lambda^2 (W_1 - W_3) + W_1 \gamma^2}{(v_*^2 \Lambda^2 + \gamma^2)^{3/2}},$$

$$\delta W_3^{(c)} = V \int' \frac{d^2 \mathbf{q}}{(2\pi)^2} \int_{-\infty}^{\infty} \frac{d\nu}{2\pi} \frac{v_*^2 |\mathbf{q}|^2 \left[ W_1 - \frac{\nu^2 v_*^2 |\mathbf{q}|^2 W_3}{(v_*^2 |\mathbf{q}|^2 + \gamma^2)^2} \right]}{(\nu^2 + v_*^2 |\mathbf{q}|^2 + \gamma^2)^2}, \quad (72)$$

$$= -V \frac{1}{8\pi} \Lambda d\Lambda \frac{v_*^2 \Lambda^2 [v_*^2 \Lambda^2 (W_1 - W_3) + W_1 \gamma^2]}{(v_*^2 \Lambda^2 + \gamma^2)^{5/2}}.$$

As for the integral in  $\delta S_{(d)}^{(2)}$  and  $\delta S_{(e)}^{(2)}$ , we need to discuss the indices of  $a$  and  $a'$ . If  $a = \alpha + 2$  and  $a' = \alpha' + 2$ , then they

contribute to the following interaction corrections

$$\delta J^{(d)} = V J \left[ \int' \frac{d^2 \mathbf{q}}{(2\pi)^2} \int_{-\infty}^{\infty} \frac{d\nu}{2\pi} \times \frac{\nu^2 v_*^4 |\mathbf{q}|^4}{(\nu^2 + v_*^2 |\mathbf{q}|^2 + \gamma^2)^2 (v_*^2 |\mathbf{q}|^2 + \gamma^2)^2} \right], \quad (73)$$

$$= V J \frac{1}{8\pi} \Lambda d\Lambda \frac{v_*^4 \Lambda^4}{(v_*^2 \Lambda^2 + \gamma^2)^{5/2}},$$

$$\delta J_+^{(e)} = -V J_+ \left[ \int' \frac{d^2 \mathbf{q}}{(2\pi)^2} \int_{-\infty}^{\infty} \frac{d\nu}{2\pi} \times \frac{\nu^2 v_*^4 |\mathbf{q}|^4}{(\nu^2 + v_*^2 |\mathbf{q}|^2 + \gamma^2)^2 (v_*^2 |\mathbf{q}|^2 + \gamma^2)^2} \right], \quad (74)$$

$$= -V J_+ \frac{1}{8\pi} \Lambda d\Lambda \frac{v_*^4 \Lambda^4}{(v_*^2 \Lambda^2 + \gamma^2)^{5/2}},$$

While if  $a = \alpha$  and  $a' = \alpha'$ , then they contribute to new interactions of the form

$$S_{J^*} = J^* \frac{1}{2} (1 + \eta \eta' s_\alpha s_{\alpha'}) \times \int_{\{k_i\}} \bar{f}_{k_3, \alpha, \eta, s} \bar{c}_{k_4, \alpha', \eta', s'} f_{k_2, \alpha', \eta', s'} c_{k_1, \alpha, \eta, s}, \quad (75)$$

$$S_{J_+^*} = -\frac{J_+^*}{2} \frac{1}{2} (1 - \eta \eta' s_\alpha s_{\alpha'}) \times \int_{\{k_i\}} (\bar{f}_{k_3, \alpha, \eta, s} \bar{f}_{k_4, \alpha', \eta', s'} c_{k_2, \alpha', \eta', s'} c_{k_1, \alpha, \eta, s} + \text{h.c.}), \quad (76)$$

which can be seen from the integrals

$$\int_0^{2\pi} \frac{d\theta_{\mathbf{q}}}{2\pi} G_{\alpha+2, \alpha}^{(c)\eta}(q) G_{\alpha'+2, \alpha'}^{(c)\eta'}(q) = \frac{\eta \eta' v_*^2 |\mathbf{q}|^2}{(\nu^2 + v_*^2 |\mathbf{q}|^2 + \gamma^2)^2} \int_0^{2\pi} \frac{d\theta_{\mathbf{q}}}{2\pi} d\theta_{\mathbf{q}} e^{i(\eta s_\alpha - \eta' s_{\alpha'}) \theta_{\mathbf{q}}}$$

$$= \frac{v_*^2 |\mathbf{q}|^2}{(\nu^2 + v_*^2 |\mathbf{q}|^2 + \gamma^2)^2} \frac{1}{2} (\eta \eta' + s_\alpha s_{\alpha'}), \quad (77)$$

and

$$\int_0^{2\pi} \frac{d\theta_{\mathbf{q}}}{2\pi} G_{\alpha+2, \alpha}^{(c)\eta}(q) G_{\alpha'+2, \alpha'}^{(c)\eta'}(-q) = \frac{-\eta \eta' v_*^2 |\mathbf{q}|^2}{(\nu^2 + v_*^2 |\mathbf{q}|^2 + \gamma^2)^2} \int_0^{2\pi} \frac{d\theta_{\mathbf{q}}}{2\pi} d\theta_{\mathbf{q}} e^{i(\eta s_\alpha + \eta' s_{\alpha'}) \theta_{\mathbf{q}}}$$

$$= \frac{-v_*^2 |\mathbf{q}|^2}{(\nu^2 + v_*^2 |\mathbf{q}|^2 + \gamma^2)^2} \frac{1}{2} (\eta \eta' - s_\alpha s_{\alpha'}), \quad (78)$$

As a result, they contribute to the orbital-valley texture factor that appears in Eqs. (75-76)

$$\left[ \frac{1}{2} (\eta \eta' + s_\alpha s_{\alpha'}) \right]^2 = \frac{1}{2} (1 + \eta \eta' s_\alpha s_{\alpha'}), \quad (79)$$

$$\left[ \frac{1}{2} (\eta \eta' - s_\alpha s_{\alpha'}) \right]^2 = \frac{1}{2} (1 - \eta \eta' s_\alpha s_{\alpha'}). \quad (80)$$

The initial conditions for these new interactions are  $J^* = J_+^* = 0$ , and the corrections from  $\delta S_{(d)}^{(2)}$  and  $\delta S_{(e)}^{(2)}$  are given by

$$\delta J^* = VJ \frac{1}{8\pi} \Lambda d\Lambda \frac{v_*^2 \Lambda^2}{(v_*^2 \Lambda^2 + \gamma^2)^{3/2}}, \quad (81)$$

$$\delta J_+^* = -VJ_+ \frac{1}{8\pi} \Lambda d\Lambda \frac{v_*^2 \Lambda^2}{(v_*^2 \Lambda^2 + \gamma^2)^{3/2}}. \quad (82)$$

In principle, one should account for all interaction terms generated during the RG flow and solve the full set of flow equations self-consistently [e.g.,  $J^*$  also generates a correction to  $\gamma$  through Eq. (55)]. However, in practice, the newly generated interactions are typically small in magnitude and can be neglected without significantly affecting the results. For example, one can approximately integrate Eqs. (81-82) by holding  $V$ ,  $J$ , and  $J_+$  fixed at their initial values to estimate the renormalized couplings  $J^*$  and  $J_+^*$ , which are found to be on the order of  $\sim 1$  meV—an order of magnitude smaller than the bare values of  $J$  and  $J_+$ .

On the other hand, the diagrams in Fig. 10 involves only  $c$ -fermions and renormalize the  $V$  term:

$$\delta S_{V(a)}^{(2)} \approx \frac{1}{2} \int_{\{k_i\}} \bar{c}_{k_3, a, \eta, s} \bar{c}_{k_4, a', \eta', s'} c_{k_2, a', \eta', s'} c_{k_1, a, \eta, s} \times \int_q' \sum_{\eta, s, a_1, a_2} G_{a_1, a_2}^{(c)\eta}(q) G_{a_2, a_1}^{(c)\eta}(q) V^2, \quad (83)$$

$$\delta S_{V(b)}^{(2)} \approx -\frac{1}{2} \int_{\{k_i\}} \bar{c}_{k_3, b, \eta, s} \bar{c}_{k_4, b', \eta', s'} c_{k_2, a', \eta', s'} c_{k_1, a, \eta, s} \times \int_q' \sum_a G_{b', b}^{(c)\eta}(q) G_{a', a}^{(c)\eta}(-q) V^2, \quad (84)$$

$$\delta S_{V(c)}^{(2)} \approx -\frac{1}{2} \int_{\{k_i\}} \bar{c}_{k_3, b, \eta, s} \bar{c}_{k_4, b', \eta', s'} c_{k_2, a', \eta', s'} c_{k_1, a, \eta, s} \times \int_q' \sum_a G_{b', b}^{(c)\eta}(q) G_{a', a}^{(c)\eta}(q) V^2, \quad (85)$$

$$\delta S_{V(d)}^{(2)} \approx -\frac{1}{2} \int_{\{k_i\}} \bar{c}_{k_3, b, \eta, s} \bar{c}_{k_4, a', \eta', s'} c_{k_2, a', \eta', s'} c_{k_1, a, \eta, s} \times \int_q' \sum_a G_{a_1, a}^{(c)\eta}(q) G_{b, a_1}^{(c)\eta}(q) V^2, \quad (86)$$

$$\delta S_{V(e)}^{(2)} \approx -\frac{1}{2} \int_{\{k_i\}} \bar{c}_{k_3, a, \eta, s} \bar{c}_{k_4, b', \eta', s'} c_{k_2, a', \eta', s'} c_{k_1, a, \eta, s} \times \int_q' \sum_a G_{a_1, a'}^{(c)\eta}(q) G_{b', a_1}^{(c)\eta}(q) V^2. \quad (87)$$

We notice that  $S_{V(b)}^{(2)} = -S_{V(c)}^{(2)}$  since the Green function is an odd function of the momentum  $G_{a', a}^{(c)\eta}(-q) = -G_{a', a}^{(c)\eta}(q)$ , so they cancel each other. The remaining diagrams corresponds to the following interaction correction

$$\delta V^{(a)} = 8V^2 \int' \frac{d^2 \mathbf{q}}{(2\pi)^2} \int_{-\infty}^{\infty} \frac{d\nu}{2\pi} \frac{-\nu^2 + 2v_*^2 |\mathbf{q}|^2 + \frac{-\nu^2 v_*^4 |\mathbf{q}|^4}{(v_*^2 |\mathbf{q}|^2 + \gamma^2)^2}}{(\nu^2 + v_*^2 |\mathbf{q}|^2 + \gamma^2)^2}, \\ = -\frac{V^2}{\pi} \frac{\gamma^4 \Lambda d\Lambda}{(v_*^2 \Lambda^2 + \gamma^2)^{5/2}}, \quad (88)$$

$$\delta V_{ab}^{(d)} = \delta V_{a'b'}^{(e)} = V^2 \int' \frac{d^2 \mathbf{q}}{(2\pi)^2} \int_{-\infty}^{\infty} \frac{d\nu}{2\pi} \times \\ \times \frac{1}{(\nu^2 + v_*^2 |\mathbf{q}|^2 + \gamma^2)^2} \left[ \begin{array}{l} -\nu^2 + v_*^2 |\mathbf{q}|^2 \quad \sim \nu e^{i\theta_{\mathbf{q}}} v_* |\mathbf{q}| \\ \sim \nu e^{-i\theta_{\mathbf{q}}} v_* |\mathbf{q}| \quad v_*^2 |\mathbf{q}|^2 + \frac{-\nu^2 v_*^4 |\mathbf{q}|^4}{v_*^2 |\mathbf{q}|^2 + \gamma^2} \end{array} \right], \quad (89)$$

$$\rightarrow \delta V^{(d,e)} = \frac{1}{2} \text{Tr}[\delta V_{ab}^{(d,e)}] = \frac{V^2}{8\pi} \frac{\gamma^4 \Lambda d\Lambda}{(v_*^2 \Lambda^2 + \gamma^2)^{5/2}}. \quad (90)$$

As a result, the total contribution from the  $c$ -fermion-only diagrams  $\propto (\gamma/v_* \Lambda)^4$  vanishes to the leading order compared to other diagrams in Fig. 9, which agrees with previous results in graphene systems [63, 64]. The resulting analytical expressions for the leading order RG flows, given in Eqs. (46-53), describe how the interplay between hybridization and Coulomb interactions shapes the low-energy effective theory of MATBG in the THF framework.

#### IV. CONCLUSION

In this work, we have developed a perturbative RG framework based on the THF model to investigate the interplay of correlations and topology in MATBG. By focusing on the experimentally relevant intermediate regime where the flat-band Coulomb interaction scale  $U$  is comparable to the hybridization strength  $\gamma$ , our work provides useful insight for understanding the evolution of low-energy parameters in a topologically nontrivial, strongly correlated moiré system.

Our RG analysis reveals that while the single-particle parameters  $v_*$  and  $\gamma$  flow upward with decreasing energy scale, the interaction strength  $U$  remains approximately constant, resulting in a decreasing ratio  $U/\gamma$ . This trend suggests that, even when starting from a regime with  $U > \gamma$ , the system may naturally flow toward a projected-limit/Mott-semimetal regime where  $U < \gamma$ .

Our RG results mirror the THF band-structure fits using the BM model: as the ratio  $w_0/w_1$  decreases, both  $\gamma$  and  $v_*$  increases (in line with Table S4 in Ref. [34] and Table S38 in Ref. [36]). For example, comparing the hybridization gap before ( $\gamma = 25$  meV) and after ( $\gamma = 33$  meV) renormalization shows that  $w_0/w_1$  shifts only from 0.8 to  $\approx 0.7$ . While this flow nudges the system toward the chiral regime, it falls well short of the exact chiral limit  $w_0/w_1 = 0$ . The finite RG window below  $v_* \Lambda_c \approx 130$  meV limits how far the parameters can run. We stress that these numbers alone do not let us declare whether the chiral or the THF framework is the better starting point. Instead, our calculation highlights a concrete link between two seemingly disparate models and may offer clues for reconciling them.

Our results show that  $U$  remains nearly constant throughout the RG flow, which may explain the consistency between its UV value and the value  $\approx 50$  meV extracted from the STM experiments [5, 9, 10, 14, 17, 33].

Compared to previous RG approaches based on the BM model [59], our THF-based formalism offers analytical transparency and computational efficiency. It allows a direct decomposition of interaction channels into physically interpretable

forms and quantitatively tracks the evolution of these couplings. Notably, we find that the exchange interaction  $J$  becomes more prominent relative to the double-hybridization term  $J_+$  as the system flows toward lower energies.

The interaction renormalization is minimal for the intermediate energy scales  $|E| > \gamma$ . The minimal effect stems from the Dirac-like density of states as discussed in several papers in graphene [65–68]. However, significant interaction renormalization can happen at lower energies. For example, an earlier study based on the single impurity model predicts that the  $J$  term becomes irrelevant away from the integer fillings for  $|E| \gg \gamma$  [50]. The Kondo interaction, which arises after projecting out local  $f$ -fermion charge fluctuation, also tends to govern the low-energy properties away from the integer fillings [49, 50]. Our work focuses on the complementary results at the intermediate energy scales, serving as a starting point and defining the bare parameters for the low-energy effective theory at scales  $|E| < U$  and providing analytical understanding to the complicated interacting MATBG systems.

In our analysis, we neglect the momentum dependence of the interactions by assuming a screened short-range Coulomb potential. This approximation is justified when the characteristic length scale of interest is much larger than the screening length, which in our case is set by the distance to the metallic gate,  $d$ . Equivalently, the relevant momenta  $|\mathbf{k}|$  must satisfy  $|\mathbf{k}| \ll 1/d$ . Since  $d \sim 10$  nm is comparable to the moiré lattice constant  $a_M \simeq 13$  nm, this condition holds for  $|\mathbf{k}| \ll 1/d \sim \Lambda_c$  within the first mBZ, justifying the neglect of umklapp processes. In contrast, when  $d \gg a_M$ , screening becomes ineffective, and the Coulomb interaction must be treated as long-range, scaling as  $1/|\mathbf{k}|$ . In this regime, both the momentum dependence of the interaction and umklapp processes must be incorporated into the RG analysis. Notably, such a treatment can generate additional interactions, such as RKKY-like couplings between the  $f$ -fermions [45, 47]. Other than gate screening, there is also screening from the electron. Electron screening may be implemented using static RPA [63], while the RG treatment of dynamically screened Coulomb interactions would require

next-to-leading-order diagrams in the RPA [69], which is beyond the scope of this paper.

While a fully self-consistent renormalization group calculation would track all interaction terms generated during the flow, in practice, these newly generated couplings—such as  $J^*$  and  $J_+^*$  defined in Eqs. (75-76)—are found to be small in magnitude  $\sim 1$  meV comparable to various other exchange terms that we ignore in the THF model [34], and can be neglected without significantly altering the results. In addition, it is likely that the higher-loop effects should be negligible since the flow is minimal for interactions.

Our RG framework is broadly applicable to other moiré systems and flat-band materials that can be effectively described by the THF model. Notable examples include magic-angle mirror-symmetric twisted trilayer graphene [70–73], which differs from MATBG by featuring an additional Dirac band in the non-interacting spectrum; the twisted checkerboard model [74–76]; and the Lieb lattice [77, 78], all of which exhibit similar flat-band structures and topological features. More generally, our formalism is adaptable to stoichiometric systems and engineered lattices that host hybridized band structures resembling those of atomic  $f$ -electrons coupled to topological semimetals [78], making it a versatile tool for exploring interaction-driven phenomena across a wide class of quantum materials. Future directions include incorporating effects of finite doping away from CNP, strain, disorder, and comparing predictions with spectroscopic and transport experiments. These efforts will be important to establishing a unified low-energy description of correlated moiré flat bands and their emergent quantum phases.

## ACKNOWLEDGMENTS

We thank Matt Foster, Jay Sau, Fengcheng Wu, and Jiabin Yu for useful discussions. This work is supported by the Laboratory for Physical Sciences.

## Appendix A: Integrals and identities related to Green functions

In this appendix, we list some useful integrals and identities related to Green functions in the diagram calculation.

### 1. Frequency integral

If  $a > 0$  and  $n > 1/2$ , then we have the integral

$$\int_{-\infty}^{\infty} \frac{d\omega}{(\omega^2 + a^2)^n} = \sqrt{\pi} \frac{a^{1-2n} \Gamma(n-1/2)}{\Gamma(n)}, \quad (\text{A1})$$

where  $\Gamma(n)$  is the Gamma function. This can be used to compute the integral appeared in many diagrams involving a product of two Green functions, for example,

$$\int_{-\infty}^{\infty} d\omega \frac{\gamma^2}{(\omega^2 + v_*^2 k^2 + \gamma^2)^2} = \frac{\pi}{2} \frac{\gamma^2}{(v_*^2 k^2 + \gamma^2)^{3/2}}. \quad (\text{A2})$$

## 2. Trace in polarization bubble

In the polarization bubble diagram such as Fig. 9 (a) and 10 (a), we encounter the trace of the Green functions

$$\begin{aligned} \sum_{a_1, a_2} G_{a_1, a_2}^{(c)\eta}(z, \mathbf{k}) G_{a_2, a_1}^{(c)\eta}(z, \mathbf{k}) W_{a_1} W_{a_2} &= \text{Tr} \left( \begin{array}{cc} \frac{W_1 (v_*^2 |\mathbf{k}|^2 W_3 + W_1 z^2)}{(\gamma^2 + v_*^2 |\mathbf{k}|^2 - z^2)^2} & \frac{\eta k v W_3 z e^{i s_\alpha \eta \theta} (v_*^2 |\mathbf{k}|^2 (W_1 + W_3) + \gamma^2 W_1)}{(\gamma^2 + v_*^2 |\mathbf{k}|^2)(\gamma^2 + v_*^2 |\mathbf{k}|^2 - z^2)^2} \\ \frac{\eta k v W_1 z e^{-i s_\alpha \eta \theta} (v_*^2 |\mathbf{k}|^2 (W_1 + W_3) + \gamma^2 W_1)}{(\gamma^2 + v_*^2 |\mathbf{k}|^2)(\gamma^2 + v_*^2 |\mathbf{k}|^2 - z^2)^2} & \frac{v_*^2 |\mathbf{k}|^2 W_3 \left( \frac{v_*^2 |\mathbf{k}|^2 W_3 z^2}{(\gamma^2 + v_*^2 |\mathbf{k}|^2)^2} + W_1 \right)}{(\gamma^2 + v_*^2 |\mathbf{k}|^2 - z^2)^2} \end{array} \right) \\ &= \frac{2v_*^2 |\mathbf{k}|^2 W_1 W_3 + \frac{v_*^4 |\mathbf{k}|^4 W_3^2 z^2}{(\gamma^2 + v_*^2 |\mathbf{k}|^2)^2} + W_1^2 z^2}{(\gamma^2 + v_*^2 |\mathbf{k}|^2 - z^2)^2}, \end{aligned} \quad (\text{A3})$$

$$\begin{aligned} \sum_{a_1, a_2} G_{a_1, a_2}^{(c)\eta}(z, \mathbf{k}) G_{a_2, a_1}^{(c)\eta}(z, \mathbf{k}) &= \frac{1}{(\gamma^2 + v_*^2 |\mathbf{k}|^2 - z^2)^2} \text{Tr} \left( \begin{array}{cc} v_*^2 |\mathbf{k}|^2 + z^2 & \frac{\eta k v z e^{i s_\alpha \eta \theta} (\gamma^2 + 2v_*^2 |\mathbf{k}|^2)}{\gamma^2 + v_*^2 |\mathbf{k}|^2} \\ \frac{\eta k v z e^{-i s_\alpha \eta \theta} (\gamma^2 + 2v_*^2 |\mathbf{k}|^2)}{\gamma^2 + v_*^2 |\mathbf{k}|^2} & v_*^2 |\mathbf{k}|^2 + \frac{v_*^4 |\mathbf{k}|^4 z^2}{(\gamma^2 + v_*^2 |\mathbf{k}|^2)^2} \end{array} \right) \\ &= \frac{2v_*^2 |\mathbf{k}|^2 + \frac{v_*^4 |\mathbf{k}|^4 z^2}{(\gamma^2 + v_*^2 |\mathbf{k}|^2)^2} + z^2}{(\gamma^2 + v_*^2 |\mathbf{k}|^2 - z^2)^2}. \end{aligned} \quad (\text{A4})$$

## 3. Integrals in self-energy diagrams

The bubble self-energy diagram involves integral  $\int_q' G_1(q)$ . Since  $G_1(q)$  is an odd function in  $q$  except for the matrix element  $G_{\alpha, \alpha}^{(cf)}(q)$  [cf. Eq. (28)], we have the following result

$$\begin{aligned} \int_q' G_1^{\alpha\eta}(q) &= \int_{\Lambda-d\Lambda}^{\Lambda} \frac{|\mathbf{q}| d|\mathbf{q}|}{2\pi} \int_{-\infty}^{\infty} \frac{d\nu}{2\pi} \int_0^{2\pi} \frac{d\theta_{\mathbf{q}}}{2\pi} G_1^{\alpha\eta}(q) \\ &= -\frac{\Lambda d\Lambda}{4\pi\sqrt{v_*^2 \Lambda^2 + \gamma^2}} \begin{bmatrix} 0 & \gamma & 0 \\ \gamma & 0 & 0 \\ 0 & 0 & 0 \end{bmatrix}. \end{aligned} \quad (\text{A5})$$

On the other hand, the exchange self energy diagram involves integral  $\int_q' G_1(q+k)$  where  $q$  is the internal momentum and  $k$  is the external momentum. To compute this integral, we expand the Green function assuming  $k \ll q$ :

$$G_1^{\alpha\eta}(z+x, \mathbf{k}+\mathbf{q}) \approx G_1^{\alpha\eta}(x, \mathbf{q}) + \begin{bmatrix} \delta G^{(f)} & \delta G^{(fc)\eta} \\ \delta G^{(cf)\eta} & \delta G^{(c)\eta} \end{bmatrix}, \quad (\text{A6})$$

where

$$\begin{aligned} \delta G^{(f)} &= \frac{-z\gamma^2(x^2 + v_*^2 |\mathbf{q}|^2 + \gamma^2)}{(v_*^2 |\mathbf{q}|^2 + \gamma^2)(-x^2 + v_*^2 |\mathbf{q}|^2 + \gamma^2)^2} + \\ &+ \frac{2x\gamma^2 v_*^2 \mathbf{k} \cdot \mathbf{q} (2\gamma^2 + 2v_*^2 |\mathbf{q}|^2 - x^2)}{(\gamma^2 + v_*^2 |\mathbf{q}|^2)^2 (-x^2 + v_*^2 |\mathbf{q}|^2 + \gamma^2)^2}, \end{aligned} \quad (\text{A7})$$

$$\begin{aligned} \delta G^{(c)\eta} &= \begin{bmatrix} \frac{-z(x^2 + v_*^2 |\mathbf{q}|^2 + \gamma^2)}{(-x^2 + v_*^2 |\mathbf{q}|^2 + \gamma^2)^2} & \frac{-2x z v_* |\mathbf{q}| \eta e^{i s_\alpha \eta \theta} \mathbf{q}}{(-x^2 + v_*^2 |\mathbf{q}|^2 + \gamma^2)^2} \\ \frac{-2x z v_* |\mathbf{q}| \eta e^{-i s_\alpha \eta \theta} \mathbf{q}}{(-x^2 + v_*^2 |\mathbf{q}|^2 + \gamma^2)^2} & \frac{-z v_*^2 |\mathbf{q}|^2 (x^2 + v_*^2 |\mathbf{q}|^2 + \gamma^2)}{(v_*^2 |\mathbf{q}|^2 + \gamma^2)(-x^2 + v_*^2 |\mathbf{q}|^2 + \gamma^2)^2} \end{bmatrix} + \\ &+ \begin{bmatrix} \frac{2x v_*^2 \mathbf{k} \cdot \mathbf{q}}{(-x^2 + v_*^2 |\mathbf{q}|^2 + \gamma^2)^2} & \frac{2v_*^3 \mathbf{k} \cdot \mathbf{q} (\eta q_x + i s_\alpha q_y)}{(-x^2 + v_*^2 |\mathbf{q}|^2 + \gamma^2)^2} - \frac{v_* |\mathbf{k}| \eta e^{i \eta s_\alpha \theta} \mathbf{k}}{-x^2 + v_*^2 |\mathbf{q}|^2 + \gamma^2} \\ \frac{2v_*^3 \mathbf{k} \cdot \mathbf{q} (\eta q_x - i s_\alpha q_y)}{(-x^2 + v_*^2 |\mathbf{q}|^2 + \gamma^2)^2} - \frac{v_* |\mathbf{k}| \eta e^{-i \eta s_\alpha \theta} \mathbf{k}}{-x^2 + v_*^2 |\mathbf{q}|^2 + \gamma^2} & \frac{2x v_*^2 \mathbf{k} \cdot \mathbf{q} (x^2 \gamma^2 + v_*^4 |\mathbf{q}|^4 - \gamma^4)}{(v_*^2 |\mathbf{q}|^2 + \gamma^2)^2 (-x^2 + v_*^2 |\mathbf{q}|^2 + \gamma^2)^2} \end{bmatrix} \end{aligned} \quad (\text{A8})$$

$$\delta G^{(fc)\eta} = \delta G^{(cf)\eta\dagger} = \left[ \frac{-2xz\gamma}{(-x^2+v_*^2|\mathbf{q}|^2+\gamma^2)^2}, \frac{-zv_*|\mathbf{q}|\eta e^{i s_\alpha \eta \theta_{\mathbf{q}}}(x^2+v_*^2|\mathbf{q}|^2+\gamma^2)}{(v_*^2|\mathbf{q}|^2+\gamma^2)(-x^2+v_*^2|\mathbf{q}|^2+\gamma^2)^2} \right] + \left[ \frac{2\gamma v_*^2 \mathbf{k} \cdot \mathbf{q}}{(-x^2+v_*^2|\mathbf{q}|^2+\gamma^2)^2}, x\gamma\eta \frac{2v_*^3(\eta q_x + i s_\alpha q_y) \mathbf{k} \cdot \mathbf{q} (-x^2+2v_*^2|\mathbf{q}|^2+2\gamma^2) - v_*(\eta k_x + i s_\alpha k_y)(\gamma^2+v_*^2|\mathbf{q}|^2)(-x^2+v_*^2|\mathbf{q}|^2+\gamma^2)}{(v_*^2|\mathbf{q}|^2+\gamma^2)^2(-x^2+v_*^2|\mathbf{q}|^2+\gamma^2)^2} \right] \quad (\text{A9})$$

Here,  $z = i\omega$  and  $x = i\nu$  represent the external and internal Matsubara frequency, respectively. To calculate the integral  $\int'_q \delta G$ , one can first compute the angle integral of  $\theta_{\mathbf{q}}$ , such that

$$\int_0^{2\pi} \frac{d\theta_{\mathbf{q}}}{2\pi} \delta G^{(f)} = \frac{-z\gamma^2(x^2+v_*^2|\mathbf{q}|^2+\gamma^2)}{(v_*^2|\mathbf{q}|^2+\gamma^2)(-x^2+v_*^2|\mathbf{q}|^2+\gamma^2)^2}, \quad (\text{A10})$$

$$\int_0^{2\pi} \frac{d\theta_{\mathbf{q}}}{2\pi} \delta G^{(c)\eta} = \begin{bmatrix} \frac{-z(x^2+v_*^2|\mathbf{q}|^2+\gamma^2)}{(-x^2+v_*^2|\mathbf{q}|^2+\gamma^2)^2} & \frac{-(-x^2+\gamma^2)v_*|\mathbf{k}|\eta e^{i\eta s_\alpha \theta_{\mathbf{k}}}}{(-x^2+v_*^2|\mathbf{q}|^2+\gamma^2)^2} \\ \frac{-(-x^2+\gamma^2)v_*|\mathbf{k}|\eta e^{-i\eta s_\alpha \theta_{\mathbf{k}}}}{(-x^2+v_*^2|\mathbf{q}|^2+\gamma^2)^2} & \frac{-zv_*^2|\mathbf{q}|^2(x^2+v_*^2|\mathbf{q}|^2+\gamma^2)}{(v_*^2|\mathbf{q}|^2+\gamma^2)(-x^2+v_*^2|\mathbf{q}|^2+\gamma^2)^2} \end{bmatrix}, \quad (\text{A11})$$

$$\int_0^{2\pi} \frac{d\theta_{\mathbf{q}}}{2\pi} \delta G^{(fc)\eta} = \begin{bmatrix} \frac{-2xz\gamma}{(-x^2+v_*^2|\mathbf{q}|^2+\gamma^2)^2} & \frac{x\gamma\eta v_*(\eta k_x + i s_\alpha k_y)(x^2\gamma^2+v_*^4|\mathbf{q}|^4-\gamma^4)}{(v_*^2|\mathbf{q}|^2+\gamma^2)^2(-x^2+v_*^2|\mathbf{q}|^2+\gamma^2)^2} \end{bmatrix}. \quad (\text{A12})$$

As a result, we have  $\int'_q \delta G$  as follows

$$\int_{\Lambda-d\Lambda}^{\Lambda} \frac{|\mathbf{q}|d|\mathbf{q}|}{2\pi} \int_{-\infty}^{\infty} \frac{d\nu}{2\pi} \int_0^{2\pi} \frac{d\theta_{\mathbf{q}}}{2\pi} \delta G^{(f)} = 0, \quad (\text{A13})$$

$$\int_{\Lambda-d\Lambda}^{\Lambda} \frac{|\mathbf{q}|d|\mathbf{q}|}{2\pi} \int_{-\infty}^{\infty} \frac{d\nu}{2\pi} \int_0^{2\pi} \frac{d\theta_{\mathbf{q}}}{2\pi} \delta G^{(c)\eta} = -\frac{\Lambda d\Lambda}{8\pi} \frac{(v_*^2\Lambda^2+2\gamma^2)}{(v_*^2\Lambda^2+\gamma^2)^{3/2}} \begin{bmatrix} 0 & v_*|\mathbf{k}|\eta e^{i\eta s_\alpha \theta_{\mathbf{k}}} \\ v_*|\mathbf{k}|\eta e^{-i\eta s_\alpha \theta_{\mathbf{k}}} & 0 \end{bmatrix}, \quad (\text{A14})$$

$$\int_{\Lambda-d\Lambda}^{\Lambda} \frac{|\mathbf{q}|d|\mathbf{q}|}{2\pi} \int_{-\infty}^{\infty} \frac{d\nu}{2\pi} \int_0^{2\pi} \frac{d\theta_{\mathbf{q}}}{2\pi} \delta G^{(fc)\eta} = [0, 0], \quad (\text{A15})$$

which leads to the exchange integral

$$\begin{aligned} \int'_q G_1^{\alpha\eta}(q+k) &\approx \int_{\Lambda-d\Lambda}^{\Lambda} \frac{|\mathbf{q}|d|\mathbf{q}|}{2\pi} \int_{-\infty}^{\infty} \frac{d\nu}{2\pi} \int_0^{2\pi} \frac{d\theta_{\mathbf{q}}}{2\pi} [G_1^{\alpha\eta}(q) + \delta G] \\ &= -\frac{\Lambda d\Lambda}{4\pi\sqrt{v_*^2\Lambda^2+\gamma^2}} \begin{bmatrix} 0 & \gamma & 0 \\ \gamma & 0 & 0 \\ 0 & 0 & 0 \end{bmatrix} - \frac{\Lambda d\Lambda}{8\pi} \frac{(v_*^2\Lambda^2+2\gamma^2)}{(v_*^2\Lambda^2+\gamma^2)^{3/2}} \begin{bmatrix} 0 & 0 & 0 \\ 0 & 0 & v_*|\mathbf{k}|\eta e^{i\eta s_\alpha \theta_{\mathbf{k}}} \\ 0 & v_*|\mathbf{k}|\eta e^{-i\eta s_\alpha \theta_{\mathbf{k}}} & 0 \end{bmatrix}. \end{aligned} \quad (\text{A16})$$

## Appendix B: RG Equations beyond the leading order

In this appendix, we provide all one-loop diagrams including subleading terms of order  $\mathcal{O}(\gamma^2/v_*^2\Lambda^2)$  and  $\mathcal{O}(\gamma^4/v_*^4\Lambda^4)$  for completeness. The first-order terms  $\delta S_I^{(1)} = \langle S_I \rangle$  correspond to the self-energy shown in Fig. 11. As mentioned in the maintext, only the exchange diagrams in Fig. 11 (a) and (c) have non-zero contribution to the self energy. The second-order term  $\delta S_I^{(2)} = -\frac{1}{2}(\langle S_I^2 \rangle - \langle S_I \rangle^2)$  corresponds to the diagrams shown in Figs. 12-15. To summarize, the one-loop RG contributions to

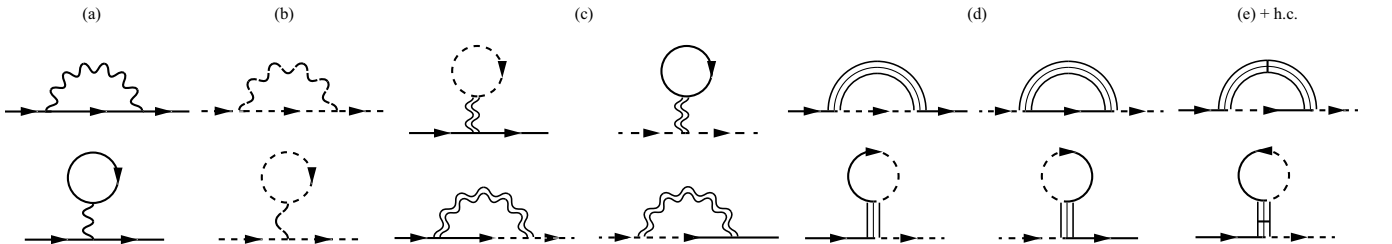


Figure 11. Renormalization to the self energy.

the interactions are given by

$$\frac{dV}{d\Lambda} = \left[ \left(1 - \frac{1}{8}\right)V^2 - V(W_1 + W_3) + \frac{1}{8}V(W_1 + W_3) + \frac{1}{4}(W_1 + W_3)^2 + \frac{1}{8}VJ - \frac{1}{32}J(W_1 + W_3) \right] \frac{\gamma^4 \Lambda}{\pi(v_*^2 \Lambda^2 + \gamma^2)^{5/2}}, \quad (\text{B1})$$

$$\begin{aligned} \frac{dU}{d\Lambda} &= \left[ (W_1 - W_3)^2 + \frac{1}{4}J(W_1 - W_3) \right] \frac{v_*^4 \Lambda^5}{\pi(v_*^2 \Lambda^2 + \gamma^2)^{5/2}} + \\ &+ \left[ -\left(2 - \frac{1}{4}\right)U(W_1 - W_3) + 2W_1(W_1 - W_3) - \frac{1}{4}UJ + \frac{1}{8}JW_1 \right] \frac{\gamma^2 v_*^2 \Lambda^3}{\pi(v_*^2 \Lambda^2 + \gamma^2)^{5/2}} + \\ &+ \left[ \left(1 - \frac{1}{4}\right)U^2 - \left(2 - \frac{1}{4}\right)UW_1 + W_1^2 \right] \frac{\gamma^4 \Lambda}{\pi(v_*^2 \Lambda^2 + \gamma^2)^{5/2}}, \end{aligned} \quad (\text{B2})$$

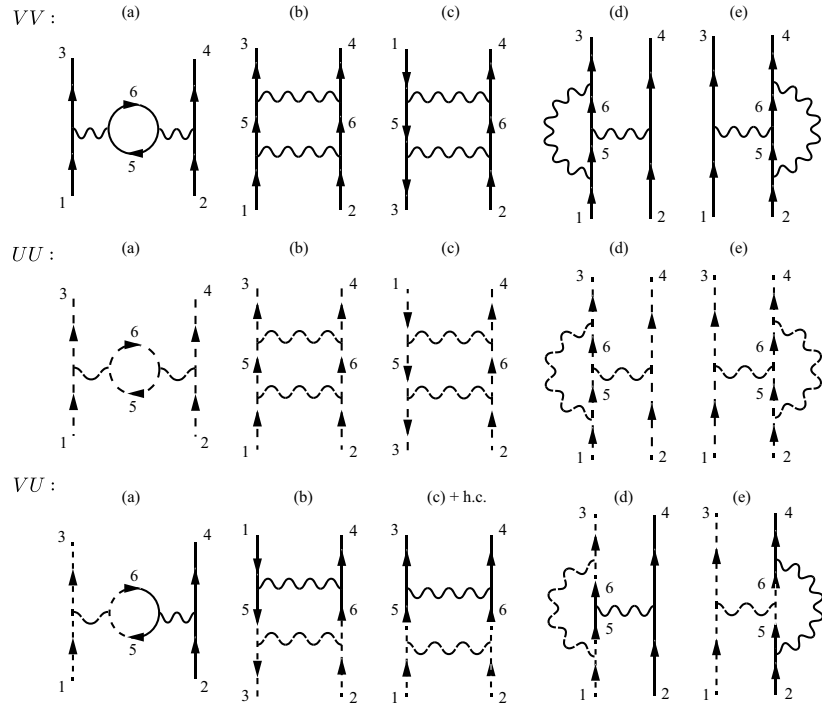
$$\begin{aligned} \frac{dW_1}{d\Lambda} &= -\frac{1}{8}V(W_1 - W_3) \frac{v_*^4 \Lambda^5}{\pi(v_*^2 \Lambda^2 + \gamma^2)^{5/2}} + \\ &+ \left[ \frac{1}{8}VU + \left(1 - \frac{1}{8}\right)V(W_1 - W_3) - \frac{1}{8}VW_1 - W_1(W_1 - W_3) + \frac{1}{8}VJ - \frac{1}{8}W_1J \right] \frac{\gamma^2 v_*^2 \Lambda^3}{\pi(v_*^2 \Lambda^2 + \gamma^2)^{5/2}} + \\ &+ \left[ -\left(1 - \frac{1}{8} - \frac{1}{8}\right)VU + \left(1 - \frac{1}{8} - \frac{1}{8}\right)VW_1 + \left(1 - \frac{1}{8}\right)UW_1 - W_1^2 \right] \frac{\gamma^4 \Lambda}{\pi(v_*^2 \Lambda^2 + \gamma^2)^{5/2}}, \end{aligned} \quad (\text{B3})$$

$$\begin{aligned} \frac{dW_3}{d\Lambda} &= \frac{1}{8}V(W_1 - W_3) \frac{v_*^4 \Lambda^5}{\pi(v_*^2 \Lambda^2 + \gamma^2)^{5/2}} + \\ &+ \left[ -\frac{1}{8}VU + V(W_1 - W_3) + \frac{1}{8}VW_1 - W_3(W_1 - W_3) + \frac{1}{8}VJ + \frac{1}{8}(W_1 - W_3)J - \frac{1}{8}W_3J \right] \frac{\gamma^2 v_*^2 \Lambda^3}{\pi(v_*^2 \Lambda^2 + \gamma^2)^{5/2}} + \\ &+ \left[ -\left(1 - \frac{1}{8}\right)VU + VW_1 + \left(1 - \frac{1}{8}\right)UW_1 - W_3W_1 - \frac{1}{8}UJ + \frac{1}{8}W_1J \right] \frac{\gamma^4 \Lambda}{\pi(v_*^2 \Lambda^2 + \gamma^2)^{5/2}}, \end{aligned} \quad (\text{B4})$$

$$\begin{aligned} \frac{dJ}{d\Lambda} &= -\frac{1}{8}VJ \frac{v_*^4 \Lambda^5}{\pi(v_*^2 \Lambda^2 + \gamma^2)^{5/2}} + \\ &+ \left[ -\frac{1}{8}VU - \frac{1}{8}W_3^2 - \left(\frac{1}{8} - \frac{1}{8} + \frac{1}{8} - \frac{1}{8}\right)W_3J - \left(\frac{1}{8} - \frac{1}{2} - \frac{1}{8}\right)J^2 - \frac{1}{2}J^2 \right] \frac{\gamma^2 v_*^2 \Lambda^3}{\pi(v_*^2 \Lambda^2 + \gamma^2)^{5/2}} + \\ &- \frac{1}{8}UJ \frac{\gamma^4 \Lambda}{\pi(v_*^2 \Lambda^2 + \gamma^2)^{5/2}}, \end{aligned} \quad (\text{B5})$$

$$\begin{aligned} \frac{dJ_+}{d\Lambda} &= \frac{1}{8}VJ_+ \frac{v_*^4 \Lambda^5}{\pi(v_*^2 \Lambda^2 + \gamma^2)^{5/2}} + \\ &+ \left[ \frac{1}{8}VU + \frac{1}{8}W_3^2 - \left(\frac{1}{4} + \frac{1}{4}\right)W_3J_+ + JJ_+ \right] \frac{\gamma^2 v_*^2 \Lambda^3}{\pi(v_*^2 \Lambda^2 + \gamma^2)^{5/2}} + \\ &+ \frac{1}{8}UJ_+ \frac{\gamma^4 \Lambda}{\pi(v_*^2 \Lambda^2 + \gamma^2)^{5/2}}. \end{aligned} \quad (\text{B6})$$

The RG contributions corresponding to diagrams shown in Fig. 12 read

Figure 12. Renormalization to the interaction terms contributed from  $VV$ ,  $UU$ , and  $VU$ .

$$VV \text{ (a): } \delta V = -V^2 \frac{1}{\pi} \Lambda d\Lambda \frac{\gamma^4}{(v_*^2 \Lambda^2 + \gamma^2)^{5/2}}, \quad (\text{B7})$$

$$VV \text{ (b)+(c)=0}, \quad (\text{B8})$$

$$VV \text{ (d)=(e): } \delta V = V^2 \frac{1}{16\pi} \Lambda d\Lambda \frac{\gamma^4}{(v_*^2 \Lambda^2 + \gamma^2)^{5/2}}, \quad (\text{B9})$$

$$UU \text{ (a): } \delta U = -U^2 \frac{1}{\pi} \Lambda d\Lambda \frac{\gamma^4}{(v_*^2 \Lambda^2 + \gamma^2)^{5/2}}, \quad (\text{B10})$$

$$UU \text{ (b)+(c)=0}, \quad (\text{B11})$$

$$UU \text{ (d)=(e): } \delta U = U^2 \frac{1}{8\pi} \Lambda d\Lambda \frac{\gamma^4}{(v_*^2 \Lambda^2 + \gamma^2)^{5/2}}, \quad (\text{B12})$$

$$VU \text{ (a): } \delta W_1 = \delta W_3 = VU \frac{1}{\pi} \Lambda d\Lambda \frac{\gamma^4}{(v_*^2 \Lambda^2 + \gamma^2)^{5/2}}, \quad (\text{B13})$$

$$VU \text{ (b): } \delta J = VU \frac{1}{8\pi} \Lambda d\Lambda \frac{v_*^2 \Lambda^2 \gamma^2}{(v_*^2 \Lambda^2 + \gamma^2)^{5/2}}, \quad (\text{B14})$$

$$VU \text{ (c) + h.c.: } \delta J_+ = -VU \frac{1}{8\pi} \Lambda d\Lambda \frac{v_*^2 \Lambda^2 \gamma^2}{(v_*^2 \Lambda^2 + \gamma^2)^{5/2}}, \quad (\text{B15})$$

$$VU \text{ (d): } \delta W_1 = \delta W_3 = -VU \frac{1}{8\pi} \Lambda d\Lambda \frac{\gamma^4}{(v_*^2 \Lambda^2 + \gamma^2)^{5/2}}, \quad (\text{B16})$$

$$VU \text{ (e): } \delta W_1 = -VU \frac{1}{8\pi} \Lambda d\Lambda \frac{\gamma^2}{(v_*^2 \Lambda^2 + \gamma^2)^{3/2}}, \quad (\text{B17})$$

$$\delta W_3 = VU \frac{1}{8\pi} \Lambda d\Lambda \frac{v_*^2 \Lambda^2 \gamma^2}{(v_*^2 \Lambda^2 + \gamma^2)^{5/2}}. \quad (\text{B18})$$

The RG contributions corresponding to diagrams shown in Fig. 13 read

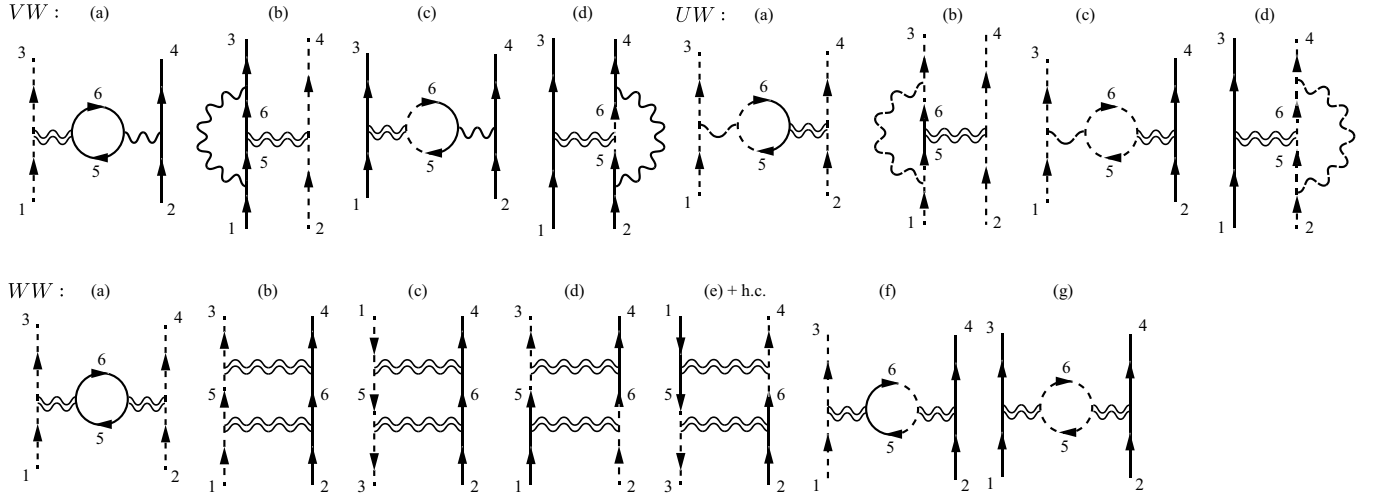


Figure 13. Renormalization to the interaction terms contributed from  $VW$ ,  $UW$ , and  $WW$ .

$$VW \text{ (a): } \delta W_1 = \delta W_3 = -V \frac{1}{\pi} \Lambda d\Lambda \frac{\gamma^2 [v_*^2 \Lambda^2 (W_1 - W_3) + W_1 \gamma^2]}{(v_*^2 \Lambda^2 + \gamma^2)^{5/2}}, \quad (\text{B19})$$

$$VW \text{ (b): } \delta W_1 = V \frac{1}{8\pi} \Lambda d\Lambda \frac{v_*^2 \Lambda^2 (W_1 - W_3) + W_1 \gamma^2}{(v_*^2 \Lambda^2 + \gamma^2)^{3/2}}, \quad (\text{B20})$$

$$\delta W_3 = -V \frac{1}{8\pi} \Lambda d\Lambda \frac{v_*^2 \Lambda^2 [v_*^2 \Lambda^2 (W_1 - W_3) + W_1 \gamma^2]}{(v_*^2 \Lambda^2 + \gamma^2)^{5/2}}, \quad (\text{B21})$$

$$VW \text{ (c): } \delta V = V (W_1 + W_3) \frac{1}{\pi} \Lambda d\Lambda \frac{\gamma^4}{(v_*^2 \Lambda^2 + \gamma^2)^{5/2}}, \quad (\text{B22})$$

$$VW \text{ (d): } \delta V = -V (W_1 + W_3) \frac{1}{8\pi} \Lambda d\Lambda \frac{\gamma^4}{(v_*^2 \Lambda^2 + \gamma^2)^{5/2}}, \quad (\text{B23})$$

$$UW \text{ (a): } \delta U = U \frac{2}{\pi} \Lambda d\Lambda \frac{\gamma^2 [v_*^2 \Lambda^2 (W_1 - W_3) + W_1 \gamma^2]}{(v_*^2 \Lambda^2 + \gamma^2)^{5/2}}, \quad (\text{B24})$$

$$UW \text{ (b): } \delta U = -U \frac{1}{4\pi} \Lambda d\Lambda \frac{\gamma^2 [v_*^2 \Lambda^2 (W_1 - W_3) + W_1 \gamma^2]}{(v_*^2 \Lambda^2 + \gamma^2)^{5/2}}, \quad (\text{B25})$$

$$UW \text{ (c): } \delta W_a = -U W_a \frac{1}{\pi} \Lambda d\Lambda \frac{\gamma^4}{(v_*^2 \Lambda^2 + \gamma^2)^{5/2}}, \quad (\text{B26})$$

$$UW \text{ (d): } \delta W_a = U W_a \frac{1}{8\pi} \Lambda d\Lambda \frac{\gamma^4}{(v_*^2 \Lambda^2 + \gamma^2)^{5/2}}, \quad (\text{B27})$$

$$WW \text{ (a): } \delta U = -\frac{1}{\pi} \Lambda d\Lambda \frac{[v_*^2 \Lambda^2 (W_1 - W_3) + W_1 \gamma^2]^2}{(v_*^2 \Lambda^2 + \gamma^2)^{5/2}}, \quad (\text{B28})$$

$$WW \text{ (b) + (c) = 0,} \quad (\text{B29})$$

$$WW \text{ (d): } \delta J = W_3^2 \frac{1}{8\pi} \Lambda d\Lambda \frac{\gamma^2 v_*^2 \Lambda^2}{(v_*^2 \Lambda^2 + \gamma^2)^{5/2}}, \quad (\text{B30})$$

$$WW \text{ (e) + h.c.: } \delta J_+ = -W_3^2 \frac{1}{8\pi} \Lambda d\Lambda \frac{\gamma^2 v_*^2 \Lambda^2}{(v_*^2 \Lambda^2 + \gamma^2)^{5/2}}, \quad (\text{B31})$$

$$WW \text{ (f): } \delta W_a = W_a \frac{1}{\pi} \Lambda d\Lambda \frac{\gamma^2 [v_*^2 \Lambda^2 (W_1 - W_3) + W_1 \gamma^2]}{(v_*^2 \Lambda^2 + \gamma^2)^{5/2}}, \quad (\text{B32})$$

$$WW \text{ (g): } \delta V = -\frac{1}{4} (W_1 + W_3)^2 \frac{1}{\pi} \Lambda d\Lambda \frac{\gamma^4}{(v_*^2 \Lambda^2 + \gamma^2)^{5/2}}. \quad (\text{B33})$$

The RG contributions corresponding to diagrams shown in Fig. 14 read

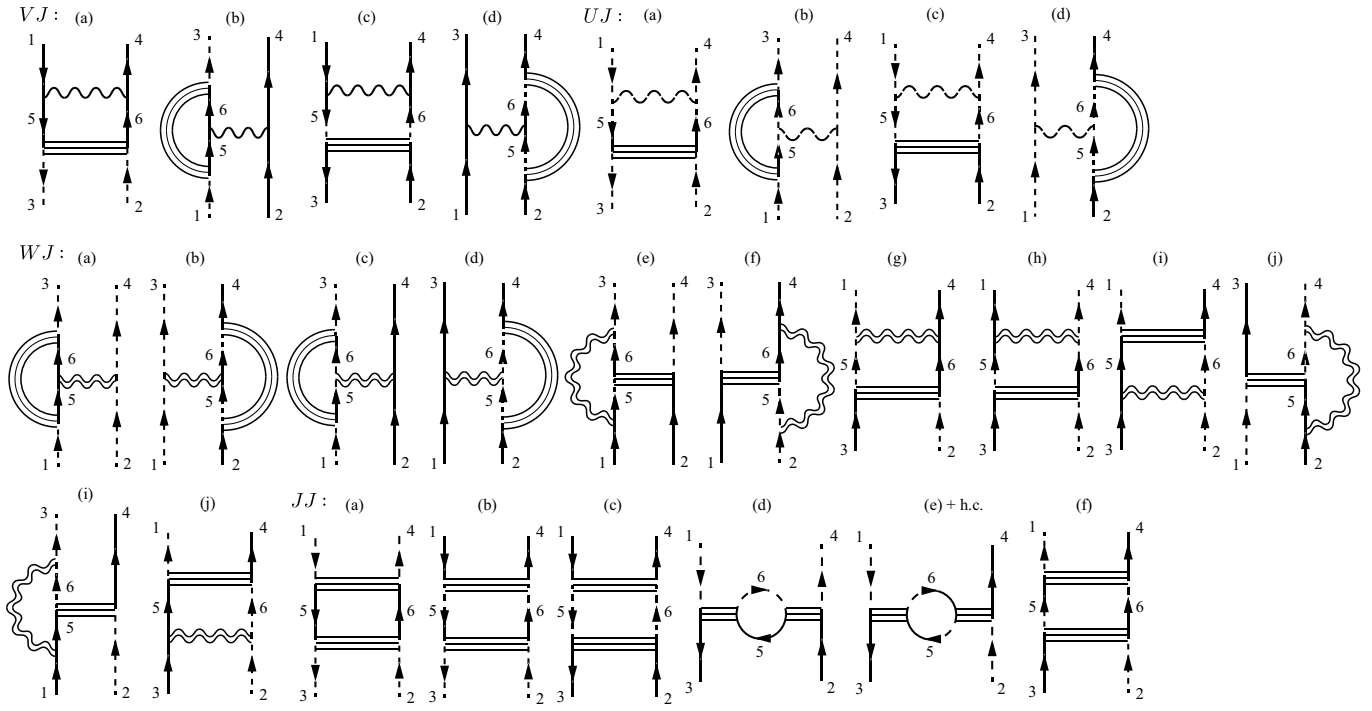


Figure 14. Renormalization to the interaction terms contributed from  $VJ$ ,  $UJ$ ,  $WJ$ , and  $JJ$ .

$$VJ \text{ (a): } \delta J = VJ \frac{1}{8\pi} \Lambda d\Lambda \frac{v_*^4 \Lambda^4}{(v_*^2 \Lambda^2 + \gamma^2)^{5/2}}, \quad (\text{B34})$$

$$VJ \text{ (b): } \delta W_1 = \delta W_3 = -VJ \frac{1}{8\pi} \Lambda d\Lambda \frac{v_*^2 \Lambda^2 \gamma^2}{(v_*^2 \Lambda^2 + \gamma^2)^{5/2}}, \quad (\text{B35})$$

$$VJ \text{ (c): New interaction} \quad (\text{B36})$$

$$VJ \text{ (d): } \delta V = -VJ \frac{1}{8\pi} \Lambda d\Lambda \frac{\gamma^4}{(v_*^2 \Lambda^2 + \gamma^2)^{5/2}}, \quad (\text{B37})$$

$$UJ \text{ (a): New interaction} \quad (\text{B38})$$

$$UJ \text{ (b): } \delta U = UJ \frac{1}{4\pi} \Lambda d\Lambda \frac{v_*^2 \Lambda^2 \gamma^2}{(v_*^2 \Lambda^2 + \gamma^2)^{5/2}}, \quad (\text{B39})$$

$$UJ \text{ (c): } \delta J = UJ \frac{1}{8\pi} \Lambda d\Lambda \frac{\gamma^4}{(v_*^2 \Lambda^2 + \gamma^2)^{5/2}}, \quad (\text{B40})$$

$$UJ \text{ (d): } \delta W_3 = UJ \frac{1}{8\pi} \Lambda d\Lambda \frac{\gamma^4}{(v_*^2 \Lambda^2 + \gamma^2)^{5/2}}, \quad (\text{B41})$$

$$WJ \text{ (a): } \delta U = -J \frac{1}{4\pi} \Lambda d\Lambda \frac{v_*^2 \Lambda^2 [v_*^2 \Lambda^2 (W_1 - W_3) + W_1 \gamma^2]}{(v_*^2 \Lambda^2 + \gamma^2)^{5/2}}, \quad (\text{B42})$$

$$WJ \text{ (b): } \delta W_3 = -J \frac{1}{8\pi} \Lambda d\Lambda \frac{\gamma^2 [v_*^2 \Lambda^2 (W_1 - W_3) + W_1 \gamma^2]}{(v_*^2 \Lambda^2 + \gamma^2)^{5/2}}, \quad (\text{B43})$$

$$WJ \text{ (c): } \delta W_a = W_a J \frac{1}{8\pi} \Lambda d\Lambda \frac{\gamma^2 v_*^2 \Lambda^2}{(v_*^2 \Lambda^2 + \gamma^2)^{5/2}}, \quad (\text{B44})$$

$$WJ \text{ (d): } \delta V = \frac{1}{2} (W_1 + W_3) J \frac{1}{16\pi} \Lambda d\Lambda \frac{\gamma^4}{(v_*^2 \Lambda^2 + \gamma^2)^{5/2}}, \quad (\text{B45})$$

$$WJ \text{ (e): } 0, \quad (\text{B46})$$

$$WJ \text{ (f): } \delta J = W_3 J \frac{1}{8\pi} \Lambda d\Lambda \frac{v_*^2 \Lambda^2 \gamma^2}{(v_*^2 \Lambda^2 + \gamma^2)^{5/2}}, \quad (\text{B47})$$

$$WJ \text{ (g): } \delta J = -W_3 J \frac{1}{8\pi} \Lambda d\Lambda \frac{v_*^2 \Lambda^2 \gamma^2}{(v_*^2 \Lambda^2 + \gamma^2)^{5/2}}, \quad (\text{B48})$$

$$WJ \text{ (h): New interactions,} \quad (\text{B49})$$

$$WJ \text{ (i): } \delta J = -W_3 J \frac{1}{8\pi} \Lambda d\Lambda \frac{v_*^2 \Lambda^2 \gamma^2}{(v_*^2 \Lambda^2 + \gamma^2)^{5/2}}, \quad (\text{B50})$$

$$WJ \text{ (j): } \delta J = W_3 J \frac{1}{8\pi} \Lambda d\Lambda \frac{v_*^2 \Lambda^2 \gamma^2}{(v_*^2 \Lambda^2 + \gamma^2)^{5/2}}, \quad (\text{B51})$$

$$JJ \text{ (a), (c): New interactions,} \quad (\text{B52})$$

$$JJ \text{ (b): } \delta J = J^2 \frac{1}{8\pi} \Lambda d\Lambda \frac{v_*^2 \Lambda^2 \gamma^2}{(v_*^2 \Lambda^2 + \gamma^2)^{5/2}}, \quad (\text{B53})$$

$$JJ \text{ (d): } \delta J = -J^2 \frac{1}{2\pi} \Lambda d\Lambda \frac{v_*^2 \Lambda^2 \gamma^2}{(v_*^2 \Lambda^2 + \gamma^2)^{5/2}}, \quad (\text{B54})$$

$$JJ \text{ (e): } 0, \quad (\text{B55})$$

$$JJ \text{ (f): } \delta J = -J^2 \frac{1}{8\pi} \Lambda d\Lambda \frac{v_*^2 \Lambda^2 \gamma^2}{(v_*^2 \Lambda^2 + \gamma^2)^{5/2}}, \quad (\text{B56})$$

$$(\text{B57})$$

The RG contributions corresponding to diagrams shown in Fig. 15 read

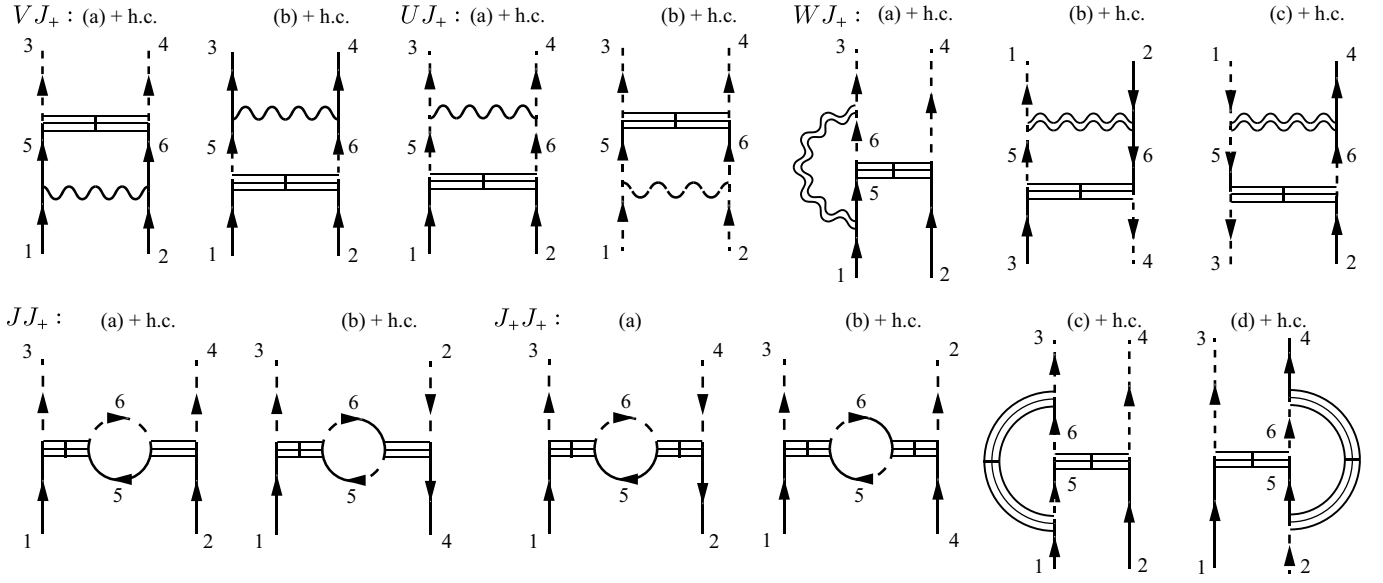


Figure 15. Renormalization to the interaction terms contributed from  $VJ_+$ ,  $UJ_+$ ,  $WJ_+$ ,  $JJ_+$ , and  $J_+J_+$ .

$$VJ_+ \text{ (a) + h.c.: } \delta J_+ = -VJ_+ \frac{1}{8\pi} \Lambda d\Lambda \frac{v_*^4 \Lambda^4}{(v_*^2 \Lambda^2 + \gamma^2)^{5/2}}, \quad (\text{B58})$$

$$VJ_+ \text{ (b) + h.c.: New interaction,} \quad (\text{B59})$$

$$UJ_+ \text{ (a) + h.c.: } \delta J_+ = -UJ_+ \frac{1}{8\pi} \Lambda d\Lambda \frac{\gamma^4}{(v_*^2 \Lambda^2 + \gamma^2)^{5/2}}, \quad (\text{B60})$$

$$UJ_+ \text{ (b) + h.c.: New interaction,} \quad (\text{B61})$$

$$WJ_+ \text{ (a) + h.c.: } \delta J_+ = W_3 J_+ \frac{1}{4\pi} \Lambda d\Lambda \frac{v_*^2 \Lambda^2 \gamma^2}{(v_*^2 \Lambda^2 + \gamma^2)^{5/2}}, \quad (\text{B62})$$

$$WJ_+ \text{ (b) + h.c.: } \delta J_+ = W_3 J_+ \frac{1}{4\pi} \Lambda d\Lambda \frac{v_*^2 \Lambda^2 \gamma^2}{(v_*^2 \Lambda^2 + \gamma^2)^{5/2}}, \quad (\text{B63})$$

$$WJ_+ \text{ (c) + h.c.: New interactions,} \quad (\text{B64})$$

$$JJ_+ \text{ (a) + h.c.: } \delta J_+ = -JJ_+ \frac{1}{\pi} \Lambda d\Lambda \frac{v_*^2 \Lambda^2 \gamma^2}{(v_*^2 \Lambda^2 + \gamma^2)^{5/2}}, \quad (\text{B65})$$

$$JJ_+ \text{ (b)=0,} \quad (\text{B66})$$

$$J_+^2 \text{ (a) + h.c.: } \delta J = -(J_+)^2 \frac{1}{2\pi} \Lambda d\Lambda \frac{v_*^2 \Lambda^2 \gamma^2}{(v_*^2 \Lambda^2 + \gamma^2)^{5/2}}, \quad (\text{B67})$$

$$J_+^2 \text{ (b), (c), (d)=0.} \quad (\text{B68})$$

- [1] Y. Cao, V. Fatemi, A. Demir, S. Fang, S. L. Tomarken, J. Y. Luo, J. D. Sanchez-Yamagishi, K. Watanabe, T. Taniguchi, E. Kaxiras, R. C. Ashoori, and P. Jarillo-Herrero, *Correlated insulator behaviour at half-filling in magic-angle graphene superlattices*, Nature **556**, 80 (2018).
- [2] Y. Cao, V. Fatemi, S. Fang, K. Watanabe, T. Taniguchi, E. Kaxiras, and P. Jarillo-Herrero, *Unconventional superconductivity in magic-angle graphene superlattices*, Nature **556**, 43 (2018).
- [3] H. Polshyn, M. Yankowitz, S. Chen, Y. Zhang, K. Watanabe, T. Taniguchi, C. R. Dean, and A. F. Young, *Large linear-*

*in-temperature resistivity in twisted bilayer graphene*, Nature Physics **15**, 1011 (2019).

- [4] A. L. Sharpe, E. J. Fox, A. W. Barnard, J. Finney, K. Watanabe, T. Taniguchi, M. A. Kastner, and D. Goldhaber-Gordon, *Emergent ferromagnetism near three-quarters filling in twisted bilayer graphene*, Science **365**, 605 (2019).

- [5] Y. Jiang, X. Lai, K. Watanabe, T. Taniguchi, K. Haule, J. Mao, and E. Y. Andrei, *Charge order and broken rotational symmetry in magic-angle twisted bilayer graphene*, Nature **573**, 91 (2019).

- [6] X. Lu, P. Stepanov, W. Yang, M. Xie, M. A. Aamir, I. Das, C. Urgell, K. Watanabe, T. Taniguchi, G. Zhang, A. Bachtold, A. H. MacDonald, and D. K. Efetov, *Superconductors, orbital magnets and correlated states in magic-angle bilayer graphene*, *Nature* **574**, 653 (2019).
- [7] M. Yankowitz, S. Chen, H. Polshyn, Y. Zhang, K. Watanabe, T. Taniguchi, D. Graf, A. F. Young, and C. R. Dean, *Tuning superconductivity in twisted bilayer graphene*, *Science* **363**, 1059 (2019).
- [8] A. Kerelsky, L. J. McGilly, D. M. Kennes, L. Xian, M. Yankowitz, S. Chen, K. Watanabe, T. Taniguchi, J. Hone, C. Dean, A. Rubio, and A. N. Pasupathy, *Maximized electron interactions at the magic angle in twisted bilayer graphene*, *Nature* **572**, 95 (2019).
- [9] Y. Xie, B. Lian, B. Jäck, X. Liu, C.-L. Chiu, K. Watanabe, T. Taniguchi, B. A. Bernevig, and A. Yazdani, *Spectroscopic signatures of many-body correlations in magic-angle twisted bilayer graphene*, *Nature* **572**, 101 (2019).
- [10] Y. Choi, J. Kemmer, Y. Peng, A. Thomson, H. Arora, R. Polski, Y. Zhang, H. Ren, J. Alicea, G. Refael, F. von Oppen, K. Watanabe, T. Taniguchi, and S. Nadj-Perge, *Electronic correlations in twisted bilayer graphene near the magic angle*, *Nature Physics* **15**, 1174 (2019).
- [11] Y. Cao, D. Chowdhury, D. Rodan-Legrain, O. Rubies-Bigorda, K. Watanabe, T. Taniguchi, T. Senthil, and P. Jarillo-Herrero, *Strange metal in magic-angle graphene with near planckian dissipation*, *Physical Review Letters* **124**, 076801 (2020).
- [12] M. Serlin, C. L. Tschirhart, H. Polshyn, Y. Zhang, J. Zhu, K. Watanabe, T. Taniguchi, L. Balents, and A. F. Young, *Intrinsic quantized anomalous hall effect in a moiré heterostructure*, *Science* **367**, 900 (2020).
- [13] H. S. Arora, R. Polski, Y. Zhang, A. Thomson, Y. Choi, H. Kim, Z. Lin, I. Z. Wilson, X. Xu, J.-H. Chu, K. Watanabe, T. Taniguchi, J. Alicea, and S. Nadj-Perge, *Superconductivity in metallic twisted bilayer graphene stabilized by  $WSe_2$* , *Nature* **583**, 379 (2020).
- [14] D. Wong, K. P. Nuckolls, M. Oh, B. Lian, Y. Xie, S. Jeon, K. Watanabe, T. Taniguchi, B. A. Bernevig, and A. Yazdani, *Cascade of electronic transitions in magic-angle twisted bilayer graphene*, *Nature* **582**, 198 (2020).
- [15] X. Liu, Z. Hao, E. Khalaf, J. Y. Lee, Y. Ronen, H. Yoo, D. H. Najafabadi, K. Watanabe, T. Taniguchi, A. Vishwanath, and P. Kim, *Tunable spin-polarized correlated states in twisted double bilayer graphene*, *Nature* **583**, 221 (2020).
- [16] Y. Cao, D. Rodan-Legrain, J. M. Park, N. F. Q. Yuan, K. Watanabe, T. Taniguchi, R. M. Fernandes, L. Fu, and P. Jarillo-Herrero, *Nematicity and competing orders in superconducting magic-angle graphene*, *Science* **372**, 264 (2021), <https://www.science.org/doi/pdf/10.1126/science.abc2836>.
- [17] Y. Choi, H. Kim, C. Lewandowski, Y. Peng, A. Thomson, R. Polski, Y. Zhang, K. Watanabe, T. Taniguchi, J. Alicea, and S. Nadj-Perge, *Interaction-driven band flattening and correlated phases in twisted bilayer graphene*, *Nature Physics* **17**, 1375 (2021).
- [18] M. Oh, K. P. Nuckolls, D. Wong, R. L. Lee, X. Liu, K. Watanabe, T. Taniguchi, and A. Yazdani, *Evidence for unconventional superconductivity in twisted bilayer graphene*, *Nature* **600**, 240 (2021).
- [19] Z. Hao, A. M. Zimmerman, P. Ledwith, E. Khalaf, D. H. Najafabadi, K. Watanabe, T. Taniguchi, A. Vishwanath, and P. Kim, *Electric field-tunable superconductivity in alternating-twist magic-angle trilayer graphene*, *Science* **371**, 1133 (2021).
- [20] H. Zhou, T. Xie, T. Taniguchi, K. Watanabe, and A. F. Young, *Superconductivity in rhombohedral trilayer graphene*, *Nature* **598**, 434 (2021).
- [21] H. Zhou, T. Xie, A. Ghazaryan, T. Holder, J. R. Ehrets, E. M. Spanton, T. Taniguchi, K. Watanabe, E. Berg, M. Serbyn, and A. F. Young, *Half- and quarter-metals in rhombohedral trilayer graphene*, *Nature* **598**, 429 (2021).
- [22] J. M. Park, Y. Cao, K. Watanabe, T. Taniguchi, and P. Jarillo-Herrero, *Tunable strongly coupled superconductivity in magic-angle twisted trilayer graphene*, *Nature* **590**, 249 (2021).
- [23] J. M. Park, Y. Cao, K. Watanabe, T. Taniguchi, and P. Jarillo-Herrero, *Flavour Hund's coupling, chern gaps and charge diffusivity in moiré graphene*, *Nature* **592**, 43 (2021).
- [24] X. Liu, Z. Wang, K. Watanabe, T. Taniguchi, O. Vafek, and J. I. A. Li, *Tuning electron correlation in magic-angle twisted bilayer graphene using Coulomb screening*, *Science* **371**, 1261 (2021).
- [25] M. Kuri, C. Coleman, Z. Gao, A. Vishnuradhan, K. Watanabe, T. Taniguchi, J. Zhu, A. H. MacDonald, and J. Folk, *Spontaneous time-reversal symmetry breaking in twisted double bilayer graphene*, *Nature Communications* **13**, 6468 (2022).
- [26] R. Su, M. Kuri, K. Watanabe, T. Taniguchi, and J. Folk, *Superconductivity in twisted double bilayer graphene stabilized by  $WSe_2$* , *Nature Materials* **22**, 1332 (2023).
- [27] M. Tanaka, J. Î.-j. Wang, T. H. Dinh, D. Rodan-Legrain, S. Zaman, M. Hays, A. Almanakly, B. Kannan, D. K. Kim, B. M. Niedzielski, K. Serniak, M. E. Schwartz, K. Watanabe, T. Taniguchi, T. P. Orlando, S. Gustavsson, J. A. Grover, P. Jarillo-Herrero, and W. D. Oliver, *Superfluid stiffness of magic-angle twisted bilayer graphene*, *Nature* **638**, 99 (2025).
- [28] J. H. Pixley and E. Y. Andrei, *Ferromagnetism in magic-angle graphene*, *Science* **365**, 543 (2019).
- [29] E. Y. Andrei and A. H. MacDonald, *Graphene bilayers with a twist*, *Nature Materials* **19**, 1265 (2020).
- [30] L. Balents, C. R. Dean, D. K. Efetov, and A. F. Young, *Superconductivity and strong correlations in moiré flat bands*, *Nature Physics* **16**, 725 (2020).
- [31] U. Zondiner, A. Rozen, D. Rodan-Legrain, Y. Cao, R. Queiroz, T. Taniguchi, K. Watanabe, Y. Oreg, F. von Oppen, A. Stern, E. Berg, P. Jarillo-Herrero, and S. Ilani, *Cascade of phase transitions and dirac revivals in magic-angle graphene*, *Nature* **582**, 203 (2020).
- [32] E. Y. Andrei, D. K. Efetov, P. Jarillo-Herrero, A. H. MacDonald, K. F. Mak, T. Senthil, E. Tutuc, A. Yazdani, and A. F. Young, *The marvels of moiré materials*, *Nature Reviews Materials* **6**, 201 (2021).
- [33] K. P. Nuckolls, R. L. Lee, M. Oh, D. Wong, T. Soejima, J. P. Hong, D. Călugăru, J. Herzog-Arbeitman, B. A. Bernevig, K. Watanabe, T. Taniguchi, N. Regnault, M. P. Zaletel, and A. Yazdani, *Quantum textures of the many-body wavefunctions in magic-angle graphene*, *Nature* **620**, 525 (2023).
- [34] Z.-D. Song and B. A. Bernevig, *Magic-angle twisted bilayer graphene as a topological heavy fermion problem*, *Phys. Rev. Lett.* **129**, 047601 (2022).
- [35] H. Shi and X. Dai, *Heavy-fermion representation for twisted bilayer graphene systems*, *Physical Review B* **106**, 245129 (2022).
- [36] D. Călugăru, M. Borovkov, L. L. H. Lau, P. Coleman, Z.-D. Song, and B. A. Bernevig, *Twisted bilayer graphene as topological heavy fermion: II. Analytical approximations of the model parameters*, *Low Temperature Physics* **49**, 640 (2023), Russian version: *Fiz. Nizk. Temp.* **49**, 703-719 (2023).
- [37] R. Bistritzer and A. H. MacDonald, *Moiré bands in twisted double-layer graphene*, *Proceedings of the National Academy of Sciences* **108**, 12233 (2011).
- [38] L. Zou, H. C. Po, A. Vishwanath, and T. Senthil, *Band structure of twisted bilayer graphene: Emergent symmetries, commensurate approximants, and wannier obstructions*, *Phys. Rev. B* **98**,

- 085435 (2018).
- [39] H. C. Po, L. Zou, T. Senthil, and A. Vishwanath, *Faithful tight-binding models and fragile topology of magic-angle bilayer graphene*, *Phys. Rev. B* **99**, 195455 (2019).
- [40] S. Carr, S. Fang, H. C. Po, A. Vishwanath, and E. Kaxiras, *Derivation of wannier orbitals and minimal-basis tight-binding hamiltonians for twisted bilayer graphene: First-principles approach*, *Phys. Rev. Res.* **1**, 033072 (2019).
- [41] Z.-D. Song, B. Lian, N. Regnault, and B. A. Bernevig, *Twisted bilayer graphene. ii. stable symmetry anomaly*, *Phys. Rev. B* **103**, 205412 (2021).
- [42] P. W. Anderson, *Localized magnetic states in metals*, *Phys. Rev.* **124**, 41 (1961).
- [43] P. W. Anderson, *A poor man's derivation of scaling laws for the kondo problem*, *Journal of Physics C: Solid State Physics* **3**, 2436 (1970).
- [44] J. Herzog-Arbeitman, J. Yu, D. Călugăru, H. Hu, N. Regnault, C. Liu, O. Vafek, P. Coleman, A. Tsvelik, Z. da Song, and B. A. Bernevig, *Topological heavy fermion principle for flat (narrow) bands with concentrated quantum geometry*, arXiv:2404.07253 [cond-mat.str-el] (2024).
- [45] H. Hu, Z.-D. Song, and B. A. Bernevig, *Projected and solvable topological heavy fermion model of twisted bilayer graphene*, arXiv:2502.14039 [cond-mat.str-el] (2025).
- [46] Y.-Z. Chou and S. D. Sarma, *Kondo lattice model in magic-angle twisted bilayer graphene*, *Physical Review Letters* **131**, 026501 (2023).
- [47] H. Hu, B. A. Bernevig, and A. M. Tsvelik, *Kondo lattice model of magic-angle twisted-bilayer graphene: Hund's rule, local-moment fluctuations, and low-energy effective theory*, *Phys. Rev. Lett.* **131**, 026502 (2023).
- [48] H. Hu, G. Rai, L. Crippa, J. Herzog-Arbeitman, D. Călugăru, T. Wehling, G. Sangiovanni, R. Valentí, A. M. Tsvelik, and B. A. Bernevig, *Symmetric kondo lattice states in doped strained twisted bilayer graphene*, *Physical Review Letters* **131**, 166501 (2023).
- [49] G.-D. Zhou, Y.-J. Wang, N. Tong, and Z.-D. Song, *Kondo phase in twisted bilayer graphene*, *Physical Review B* **109**, 045419 (2024).
- [50] Y.-Z. Chou and S. D. Sarma, *Scaling theory of intrinsic kondo and hund's rule interactions in magic-angle twisted bilayer graphene*, *Physical Review B* **108**, 125106 (2023).
- [51] P. Coleman, *Introduction to Many-Body Physics* (Cambridge University Press, 2015) [See Section 8.5.2, 16.4.2, and 17.6].
- [52] Y. Li, B. M. Fregoso, and M. Dzero, *Topological mixed valence model in magic-angle twisted bilayer graphene*, *Phys. Rev. B* **110**, 045123 (2024).
- [53] L. L. H. Lau and P. Coleman, *Topological mixed valence model for twisted bilayer graphene*, *Phys. Rev. X* **15**, 021028 (2025).
- [54] J.-Y. Zhao, B. Zhou, and Y.-H. Zhang, *Mixed valence mott insulator and composite excitation in twisted bilayer graphene*, arXiv:2507.00139 [cond-mat.str-el] (2025).
- [55] P. J. Ledwith, J. Dong, A. Vishwanath, and E. Khalaf, *Non-local moments in the chern bands of twisted bilayer graphene*, arXiv:2408.16761 [cond-mat.str-el] (2024).
- [56] J.-Y. Zhao, B. Zhou, and Y.-H. Zhang, *Ancilla theory of twisted bilayer graphene i: topological mott semimetal and symmetric pseudogap metal*, arXiv:2502.17430 [cond-mat.str-el] (2025).
- [57] A gap generally opens away from CNP when particle-hole symmetry is broken. At CNP, the gap at  $\Gamma$  can also open in the presence of finite mass terms ( $M$ ), exchange interaction ( $J$ ), or external magnetic fields. Moreover, gapless behavior also emerges in the  $U \gg \gamma$  limit under the chiral flat limit ( $M, v_* \rightarrow 0$ ) [45] and within one-shot Hartree-Fock treatments assuming interaction-induced symmetry breaking [34].
- [58] G. Rai, L. Crippa, D. Călugăru, H. Hu, F. Paoletti, L. de' Medici, A. Georges, B. A. Bernevig, R. Valentí, G. Sangiovanni, and T. Wehling, *Dynamical correlations and order in magic-angle twisted bilayer graphene*, *Phys. Rev. X* **14**, 031045 (2024).
- [59] O. Vafek and J. Kang, *Renormalization group study of hidden symmetry in twisted bilayer graphene with coulomb interactions*, *Phys. Rev. Lett.* **125**, 257602 (2020).
- [60] Theoretically  $\Lambda$  can be taken as  $+\infty$  to get a full continuum model that contains all higher remote bands, although they do not match the higher remote bands in the BM model.
- [61] While incorporating extended moiré Brillouin zones beyond the first is required for quantitatively reproducing the Bistritzer-MacDonald minibands [34, 35, 45], the key qualitative features discussed here remain entirely unaffected by this approximation keeping only the first mBZ.
- [62] Adding small bandwidth  $M$ , which is a matrix element between  $c_3$  and  $c_4$  fermions, breaks such symmetry and hybridizes  $C = \pm 1$  Chern bands.
- [63] M. S. Foster and I. L. Aleiner, *Graphene via large  $n$ : A renormalization group study*, *Phys. Rev. B* **77**, 195413 (2008).
- [64] O. Vafek and K. Yang, *Many-body instability of coulomb interacting bilayer graphene: Renormalization group approach*, *Phys. Rev. B* **81**, 041401 (2010).
- [65] J. González, F. Guinea, and M. Vozmediano, *Non-fermi liquid behavior of electrons in the half-filled honeycomb lattice (a renormalization group approach)*, *Nuclear Physics B* **424**, 595 (1994).
- [66] O. Vafek, *Anomalous thermodynamics of coulomb-interacting massless dirac fermions in two spatial dimensions*, *Phys. Rev. Lett.* **98**, 216401 (2007).
- [67] D. E. Sheehy and J. Schmalian, *Quantum critical scaling in graphene*, *Phys. Rev. Lett.* **99**, 226803 (2007).
- [68] E. Barnes, E. H. Hwang, R. E. Throckmorton, and S. Das Sarma, *Effective field theory, three-loop perturbative expansion, and their experimental implications in graphene many-body effects*, *Phys. Rev. B* **89**, 235431 (2014).
- [69] J. Hofmann, E. Barnes, and S. Das Sarma, *Why does graphene behave as a weakly interacting system? Phys. Rev. Lett.* **113**, 105502 (2014).
- [70] J. Yu, M. Xie, B. A. Bernevig, and S. D. Sarma, *Magic-angle twisted symmetric trilayer graphene as a topological heavy-fermion problem*, *Physical Review B* **108**, 035129 (2023).
- [71] H. Kim, Y. Choi, C. Lewandowski, A. Thomson, Y. Zhang, R. Polski, K. Watanabe, T. Taniguchi, J. Alicea, and S. Nadj-Perge, *Evidence for unconventional superconductivity in twisted trilayer graphene*, *Nature* **606**, 494 (2022).
- [72] A. Banerjee, Z. Hao, M. Kreidel, P. Ledwith, I. Phinney, J. M. Park, A. Zimmerman, M. E. Wesson, K. Watanabe, T. Taniguchi, R. M. Westervelt, A. Yacoby, P. Jarillo-Herrero, P. A. Volkov, A. Vishwanath, K. C. Fong, and P. Kim, *Superfluid stiffness of twisted trilayer graphene superconductors*, *Nature* **638**, 93 (2025).
- [73] J. M. Park, S. Sun, K. Watanabe, T. Taniguchi, and P. Jarillo-Herrero, *Simultaneous transport and tunneling spectroscopy of moiré graphene: Distinct observation of the superconducting gap and signatures of nodal superconductivity*, arXiv:2503.16410 [cond-mat.supr-con] (2025).
- [74] M.-R. Li, A.-L. He, and H. Yao, *Magic-angle twisted bilayer systems with quadratic band touching: Exactly flat bands with high chern number*, *Phys. Rev. Res.* **4**, 043151 (2022).
- [75] S. Sarkar, X. Wan, S.-Z. Lin, and K. Sun, *Symmetry-based classification of exact flat bands in single and bilayer moiré systems*, arXiv:2310.02218 [cond-mat.mes-hall] (2023).

- [76] J.-Z. Ma, R.-Z. Huang, G.-Y. Zhu, J.-Y. Chen, and D.-X. Yao, *Fractional chern insulator candidate on a twisted bilayer checkerboard lattice*, *Phys. Rev. B* **110**, 165142 (2024).
- [77] E. H. Lieb, *Two theorems on the hubbard model*, *Phys. Rev. Lett.* **62**, 1201 (1989).
- [78] J. Herzog-Arbeitman, J. Yu, D. Călugăru, H. Hu, N. Regnault, C. Liu, O. Vafek, P. Coleman, A. Tsvelik, Z. da Song, and B. A. Bernevig, *Topological heavy fermion principle for flat (narrow) bands with concentrated quantum geometry*, arXiv:2404.07253 [cond-mat.str-el] (2024).